AD_____

Award Number: DAMD17-99-1-9429

TITLE: Automatic Exposure Control Device for Digital Mammography

PRINCIPAL INVESTIGATOR: Laurie L. Fajardo, M.D.

CONTRACTING ORGANIZATION: Johns Hopkins University
                            Baltimore, Maryland   21218

REPORT DATE: August 2000

TYPE OF REPORT: Annual

PREPARED FOR: U.S. Army Medical Research and Materiel Command
                Fort Detrick, Maryland   21702-5012

DISTRIBUTION STATEMENT: Approved for Public Release;
                          Distribution Unlimited

The views, opinions and/or findings contained in this report are
those of the author(s) and should not be construed as an official
Department of the Army position, policy or decision unless so
designated by other documentation.

20010727 068

REPORT DOCUMENTATION PAGE			Form Approved OMB No. 074-0188

Public reporting burden for this collection of information is estimated to average 1 hour per response, including the time for reviewing instructions, searching existing data sources, gathering and maintaining the data needed, and completing and reviewing this collection of information. Send comments regarding this burden estimate or any other aspect of this collection of information, including suggestions for reducing this burden to Washington Headquarters Services, Directorate for Information Operations and Reports, 1215 Jefferson Davis Highway, Suite 1204, Arlington, VA 22202-4302, and to the Office of Management and Budget, Paperwork Reduction Project (0704-0188), Washington, DC 20503

1. AGENCY USE ONLY (Leave blank)	2. REPORT DATE August 2000	3. REPORT TYPE AND DATES COVERED Annual (1 Aug 99 - 31 Jul 00)	
4. TITLE AND SUBTITLE Automatic Exposure control Device for Digital Mammography		5. FUNDING NUMBERS DAMD17-99-1-9429	
6. AUTHOR(S) Laurie L. Fajardo, M.D.			
7. PERFORMING ORGANIZATION NAME(S) AND ADDRESS(ES) Johns Hopkins University Baltimore, Maryland 21218 E-Mail: lfajardo@jhmi.edu		8. PERFORMING ORGANIZATION REPORT NUMBER	
9. SPONSORING / MONITORING AGENCY NAME(S) AND ADDRESS(ES) U.S. Army Medical Research and Materiel Command Fort Detrick, Maryland 21702-5012		10. SPONSORING / MONITORING AGENCY REPORT NUMBER	

11. SUPPLEMENTARY NOTES
This report contains colored photos

12a. DISTRIBUTION / AVAILABILITY STATEMENT Approved for Public Release; Distribution Unlimited	12b. DISTRIBUTION CODE

13. ABSTRACT *(Maximum 200 Words)*

Purpose: The broad, long-term objective of this IDEA proposal is to achieve optimized image quality for DM within acceptable limits of radiation exposure by developing innovative approaches for controlling DM exposures.

Scope: This project's specific aims are (1) to use short, low dose pre-exposures of the breast to create "intelligent" regions of interest that determine the exposure parameters for the fully exposed image; and (2) to select exposure parameters (mAs, kVp, and beam filtration) based on "intelligent decisions" that optimize signal-to-noise (SNR) as a function of mean glandular dose.

Major Findings & Results: Complete analysis of beam optimization for digital mammography and mean glandular dose measurements have been completed. Software has been developed for analysis of digitally acquired mammograms allowing the area greatest radiographic attenuation (the ECROI) to be selected and the pixel variance in the ECROI to be analyzed. We are currently completing running our analysis tools using digital mammograms obtained from breasts with a variety of compositions and sizes. We will evaluate the effect of radiographic heterogeneity on the selection of the ECROI, as well as possible spurious results from microcalcification clusters or cysts.

Significance: We have implemented an early version of automatic exposure control device that will be refined over the remaining 6 months of funding. Results from a pilot evaluation demonstrate that the AEC produces digital images of higher quality than current conventional mammography at similar or reduced mean glandular radiation doses.

14. SUBJECT TERMS digital mammography, automatic exposure control device, CTR, Breast cancer			15. NUMBER OF PAGES 39
			16. PRICE CODE
17. SECURITY CLASSIFICATION OF REPORT Unclassified	18. SECURITY CLASSIFICATION OF THIS PAGE Unclassified	19. SECURITY CLASSIFICATION OF ABSTRACT Unclassified	20. LIMITATION OF ABSTRACT Unlimited

NSN 7540-01-280-5500

Standard Form 298 (Rev. 2-89)
Prescribed by ANSI Std. Z39-18
298-102

Table of Contents

Introduction

The broad, long-term objective of this IDEA proposal is to achieve optimized image quality for DM within acceptable limits of radiation exposure by developing innovative approaches for controlling DM exposures. These approaches entail using the digital detector and an artificial neural network to control mammographic exposures. This project's specific aims are (1) to use short, low dose pre-exposures of the breast to create "intelligent" regions of interest that determine the exposure parameters for the fully exposed image; and (2) to use an artificial neural network to select exposure parameters (mAs, kVp, and beam filtration) based on "intelligent decisions" that optimize signal-to-noise (SNR) as a function of mean glandular dose.

Body: Progress on Research Tasks & Key Research Accomplishments

Task 1. Determine optimal pixel binning factor and size of exposure-controlling ROI.

The ideal exposure-controlling ROI (ECROI) is large enough so that small, high-density structures such as calcifications are not selected to determine exposure parameters, but small enough so that the image is not smoothed excessively. To determine an optimal ECROI size, we surveyed FFDM images from our clinical image database, evaluating 3-D surface plots to determine where the "peaks" of low exposure areas are located and the range of the super-pixel values in the peaks. This provided information on the effects of the location and size of the ECROI. We evaluated the effect of the ECROI size on the calculation of the SNR (Figures 1-7). Next, we developed software to analyze selected ROIs (super-pixels) of digitally acquired mammograms. The primary two questions to be addressed by these analysis tools are:

1) Which area of the digitally obtained mammogram contains the area of greatest radiographic attenuation (the ECROI)?
2) What portion of the pixel variance in the ECROI is a result of differential breast attenuation (signal) as opposed to random fluctuations (noise)?

With respect to question 1), the immediate objectives of the software programs are:

a) Evaluate the correlation between the number of regions of interest (ROIs) sampled and the correct identification of the ROI containing the area of greatest radiographic attenuation (the ECROI)

b) Evaluate the correlation between ROI size and correct identification of the ECROI

c) Examine the effect of pixel binning on correct identification of the ECROI

The selection of the pixel binning factor involves tradeoffs between readout speed and information loss. We evaluated binning factors of 8 (to form 320μ x 320μ super-pixels) and 16 (giving 640μ x 640μ super-pixels) using images of the test phantom acquired at low exposures. Three-dimensional pixel-value surface plots were compared to similarly

4

binned plots made using full exposures (Figures 1-4). The location of areas having low ADU values was the same in the low- and high-exposure plots, indicating that these binning factors did not result in unacceptable image smoothing. We then examined ROIs of 800 x 800 pixels (3200µ X 3200µ pixels) (Figures 5-7) and 1600 x 1600 pixels (64,000µ X 64,000µ super-pixels). For the 3200µ X 3200µ pixel ROI, a 6 x 8 grid of ROIs was established. In our experiments (Figures 5 & 6), the ROI positions were held fixed while their side lengths varied between minimum values of approximately 1.7% of the short dimension of the image, to their maximum value, equal to the center-to-center ROI spacing. Average pixel value in the 48 ROIs (Figure 5) were plotted as a function of ROI side length, in units of binned pixels (Figure 6). We then performed similar experiments for 64K µ X 64K µ ROIs. These data were then utilized for task 2 experiments (below) to calculate the contribution of signal to the total variance of the ECROIs.

Task 2. Identify the contribution of signal to the total variance in the ECROI.

This entails distinguishing between contributions to the variance within the ECROI from breast structure and from noise (e.g., x-ray quantum noise or $\sigma_{quantum}$, and additive/system noise or σ_e) in the pre-exposure images. We have used two pre-exposures to permit pixel fluctuations arising from the signal relating to breast structure to be distinguished from those arising from noise. The ECROI is determined from the first pre-exposure. Only detector modules containing the ECROI are read out on the second pre-exposure. Pre-exposure times and initial kVp are scaled according to compressed breast thickness ($\geq$6.5 cm:30 kVp; 6 cm:29 kVp; 5.5 cm:28 kVp; 5 cm:27 kVp; 4.5 cm:26 kVp; $\leq$4.0 cm:25 kVp). Initial choices for pre-exposure times and kVp are based on values calculated to result in a MGD of approximately 150 mrads to a 50% fat / 50% fibroglandular breast in an exposure time of approximately 1 sec.

Criteria for optimization of tube voltage and external filtration in digital mammography differ from those used in screen-film mammography. This is because the separation of the processes of acquisition and display in the former permits contrast of individual structures to be adjusted when the image is displayed. It is therefore possible to detect objects with low subject contrast provided that the image signal to noise ratio (SNR) is adequate. Thus, rather than maximization of contrast within the constraints of acceptable film darkening and patient dose, beam optimization in digital mammography requires maximization of the image SNR, constrained by acceptable patient dose.

To identify optimum technique factors, the following figure of merit was used:
$$FOM = (SNR)^2/MGD,$$
Where MGD is mean dose to the glandular portion of the breast, and the SNR is Rose's suggested minimum value of 5 [1].

Using simple phantoms with known signals (disks, holes, etc.) that result in signal-induced variances that are easily determined, we calculated the ECROI SNR. Breast tissue equivalent material corresponding to 3 different fat/glandular ratios was used to simulate a range of breast thicknesses and densities. Look-up tables were generated with starting pre-exposure time and kVp for varying breast composition/thickness (288 test conditions) as input data. These data were further refined in task 3 experiments using

5

anthropomorphic breast phantoms that more closely approximate the spectral content of human breast tissue (see below).

Task 3. **Determine how breast structure relates to measured variances.** We selected a broad range of breast thickness and radiodensity from our Digital mammography patient image database to empirically determine the contribution to the total variance that arises from breast structure (signal). In order to obtain the best possible estimate of the variance associated with normal breast parenchyma, we selected ROIs from sub-areas of mammograms with obviously high SNR. In those ROIs, the average pixel value and system gain was used to calculate the x-ray quantum variance, $\sigma^2_{quantum}$. Using the measured system noise, σ_e, the contribution to the total variance, σ^2_{total}, from breast tissue was calculated from:.

$$\sigma^2_{signal} = \sigma^2_{total} - \sigma^2_{quantum} - \sigma^2_e$$

After the 2 pre-pulses, we calculated σ^2_{noise} and σ^2_{signal} and used the empirically determined relationship between σ^2_{signal} and $I_{max} - I_{min}$ to infer the magnitude of the signal. The ratio of the inferred signal to σ_{noise} is the SNR following the pre-exposure. This was then used to select exposure parameters for the full exposure. If only the exposure *time* is to be selected (phototiming mode), this is straightforward since $I_{max} - I_{min}$ is directly proportional to mAs and since the quantum noise, σ_q, increases as the square root of the exposure time. In the CCD-based TREX system, the system noise (σ_e) increases as the square root of the exposure time because of the accumulation of thermal electrons in the CCD pixels. This noise was previously characterized over a large range of exposure times.

Results of Phantom Experiments Performed for Tasks 2 & 3:
Following are example plots of measured signal, SNR, and the FOM, as a function of kVp, for a 70/30 fibroglandular/fat equivalent phantom composition, using the signal from the microcalcification-equivalent material. These data were obtained from the DM system at Johns Hopkins. The results of these studies were presented at the 5th International Workshop on Digital Mammography, Toronto, CA, June 11-14, 2000.
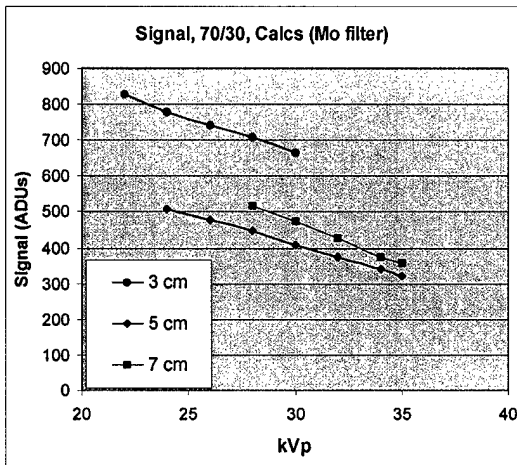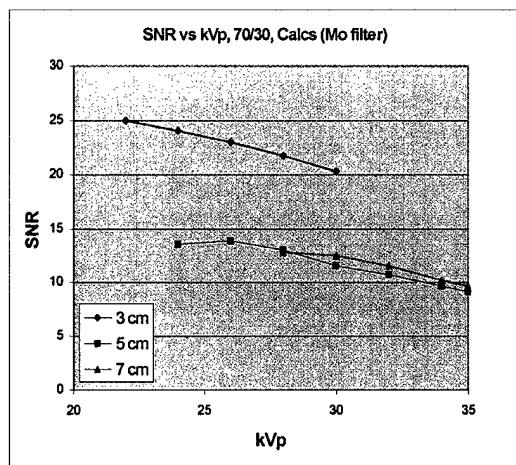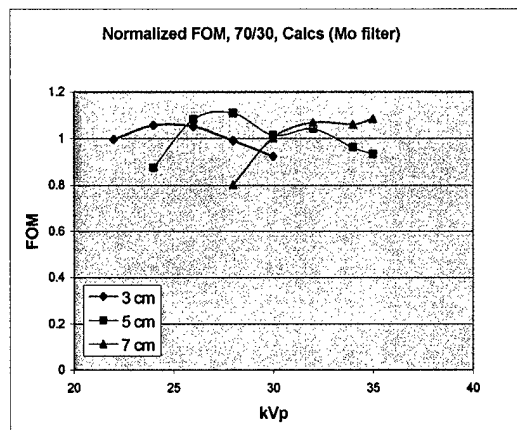
Figure 1

Figure 2

Figure 3

Nine different phantoms were assembled to simulate breasts of three different thicknesses (3 cm, 5 cm, and 7 cm), and three different attenuation equivalent adipose/fibroglandular mass ratios (30/70, 50/50, and 70/30). All blocks of a given phantom had the same adipose /fibroglandular ratio, except for two 5 mm thick blocks, common to all phantoms, that are 100% adipose equivalent. These blocks were placed at the top and bottom of the stack to simulate skin (see figure 4). In each phantom stack assembled, the centrally located block in the stack (the signal block) contained a series of test objects. For the data reported here, the test objects of interest were two stepwedges, one each of calcification equivalent and mass equivalent material. The mass equivalent stepwedge has the same x-ray attenuation as 100% glandular equivalent material, and the microcalcification equivalent step wedge is composed of calcium carbonate. Figure 5 is a schematic of a signal block showing the dimensions of the block and step wedges (other test objects present in the signal block have been omitted for clarity). The thickness of all signal blocks is 2 cm. Images were obtained in manual mode with the phantoms positioned at

7

the chest wall edge of the receptor, centered left to right. Exposure time was selected to give approximately the same average pixel value in the phantom background area for each phantom/technique combination. For each combination two images were obtained with identical exposure times for the purpose of image subtraction, taking care not to move the phantom between the two exposures. At each site, entrance exposures (mR/mAs) and half value layers (HVLs) were measured for each target/filter/kVp combination used.
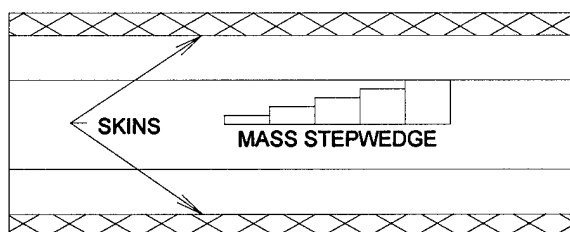

Figure 4: Side view of a 5 cm thick phantom, comprised of one 2 cm thick signal block, two 1 cm thick blank blocks, and two 0.5 cm thick skins.
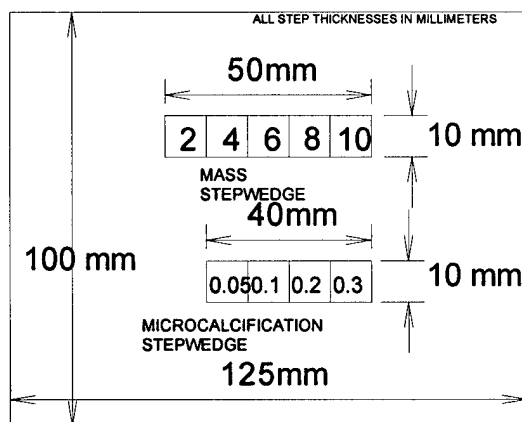

Figure 5: Schematic diagram of a signal block

ECROI Analysis:

Signal was defined as the difference between the average pixel values in a region of interest (ROI) centered on an individual step (but not including the step boundaries), and an equal sized ROI located immediately adjacent to the step, but containing only background. To quantify the image noise, the two images of a given phantom, obtained at a common technique, were subtracted. Image subtraction was performed to remove fixed pattern noise associated with phantom defects, detector non-uniformity, and the heel effect. Noise in a single image was defined as the rms pixel-to-pixel fluctuations in an ROI of 1109 x 511 pixels in the difference image, divided by the square root of two.

Evaluation of acceptable mean glandular dose:

The MGD for each phantom was calculated using its known thickness and composition, and the measured HVL and mR/mAs values from each DM system. For Mo/Mo and Mo/Rh spectra, the parameterized dose tables of Sobol and Wu were utilized to obtain the glandular dose per unit exposure [2]. For the W/Al spectra, normalized (to entrance exposure) MGD values were obtained from the data of Stanton et al. [3]. Their data were extrapolated to 3 cm breast thickness, and interpolation between their published HVL curves was used to obtain correction factors for the particular glandular volume fractions (0.22, 0.40, and 0.61, corresponding to glandular mass fractions of 0.30, 0.50, and 0.70, respectively) used in our study. For the W/Rh spectra, the calculations of Boone were utilized, interpolating between his published HVL and adipose/fibroglandular composition values [4]. All FOM values were obtained by dividing the square of the SNR by the MGD, expressed in units of 10^{-5} Gy (1 mrad).

The measured HVL values for the seven specific target/filter combinations tested at the three sites, as a function of kVp, are shown in Figure 3. Figure 4 shows the corresponding normalized MGD, D_{gN}, calculated for each of the seven spectra, plotted versus the measured HVL. Similarly, Figure 8 shows D_{gN} for each target/filter combination tested, plotted versus kVp. The general tradeoff between loss of contrast and reduction in MGD with increasing kVp is illustrated in Figure 9. In this example, the measured contrast of the 0.3 mm thick (thickest) calcification step in shown for the 5 cm thick, 50/50 phantom.

SNR versus kVp, and the corresponding FOM values vs. kVp have been determined. Figures 10 and 11 show the results obtained for the 300 micron thick step of the calcification stepwedge in the three 50/50 composition phantoms. To illustrate the applicability of these data to objects, the dependence of the FOM on the step thickness for both types of stepwedges is presented in Figures 12 and 13. These data are from images obtained using a Mo/Mo target/filter combination to image a 5 cm thick, 50/50 composition phantom. Finally, Figures 14-16 illustrate the effect on the FOM of changing breast composition, holding breast thickness fixed. Signals were calculated using the 10 mm thick mass equivalent step.
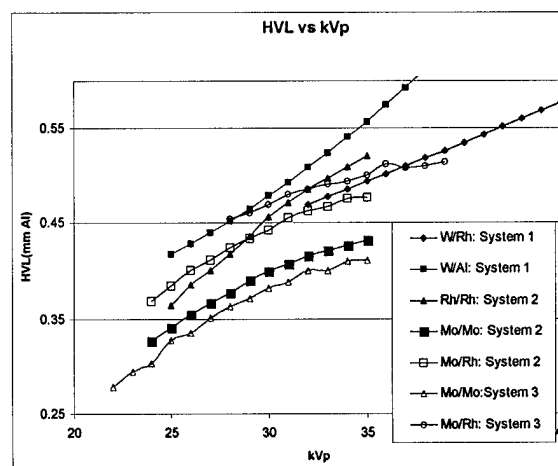

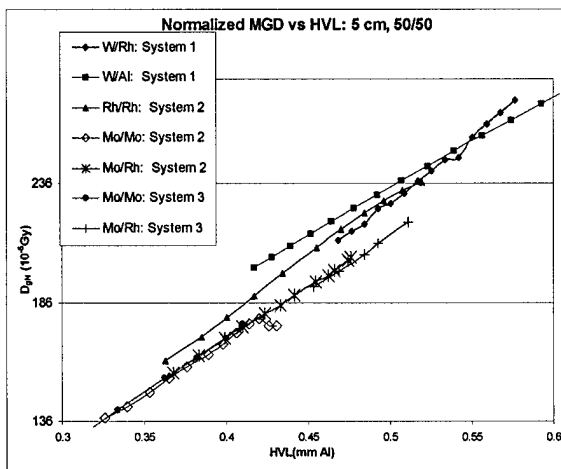Figure 6: Measured HVLs , plotted versus

9

Normalized MGD vs HVL: 5 cm, 50/50

Legend:
- W/Rh: System 1
- W/Al: System 1
- Rh/Rh: System 2
- Mo/Mo: System 2
- Mo/Rh: System 2
- Mo/Mo: System 3
- Mo/Rh: System 3

Y-axis: D_{gN} (10^{-2}Gy)
X-axis: HVL (mm Al)

Figure 7: Normalized mean glandular dose versus HVL, assuming a 5 cm thick, 50/50phantom

Normalized MGD vs kVp : 5 cm,50/50

Legend:
- W-Rh: System 1
- W-Al: System 1
- Rh-Rh: System 2
- Mo-Mo: System 2
- Mo-Rh: System 2
- Mo-Mo: System 3
- Mo-Rh: System 3

Y-axis: D_{gN} (mrad/R)
X-axis: kVp
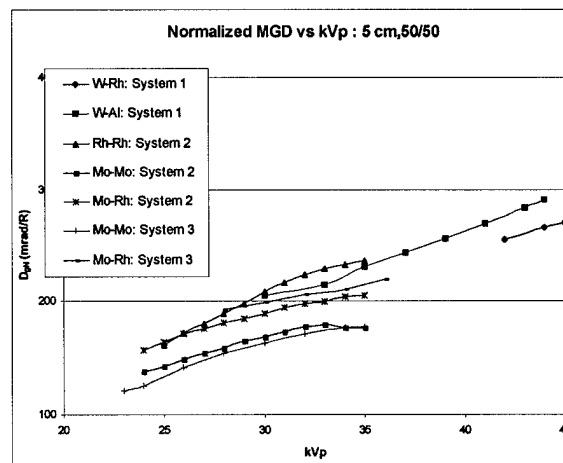
Figure 8: Normalized mean glandular dose vs. kVp assuming a 5 cm thick, 50/50 phantom

Dose and Contrast vs kVp

Y-axis (left): Contrast
Y-axis (right): DgN (10^{-2}Gy)
X-axis: kVp

Legend:
- Mo/Mo-Contrast
- Mo/Rh-Contrast
- Rh/Rh-Contrast
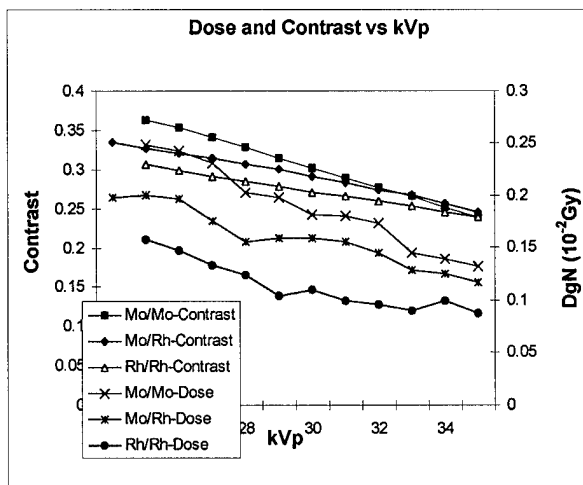- Mo/Mo-Dose
- Mo/Rh-Dose
- Rh/Rh-Dose

Figure 9: Dose and contrast versus kVp using the 0.3 mm calcification step in a 5 cm thick, 50/50 phantom
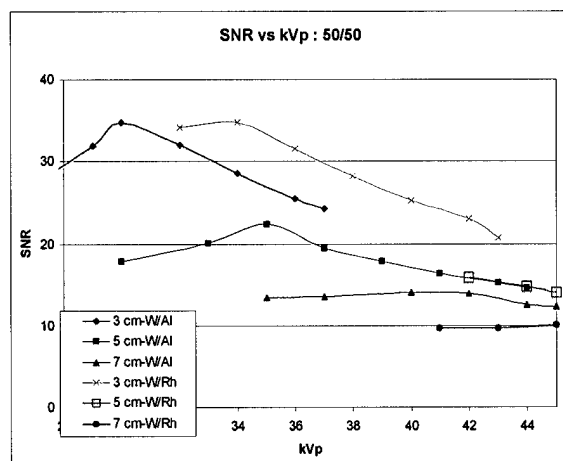
10
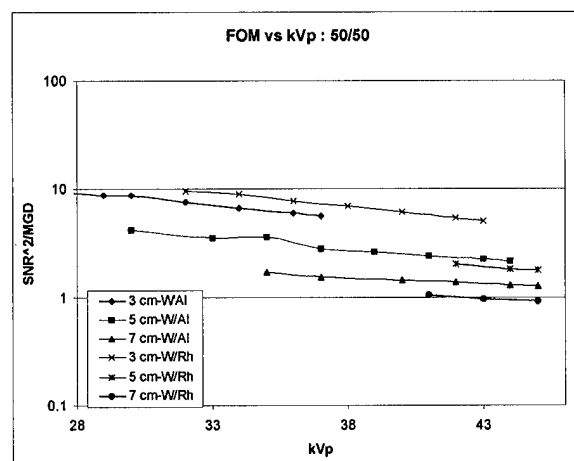
Figure 10: SNR vs. kVp.

Figure 11: FOM vs. kVp.

Figure 12: FOM values for the five steps of the mass stepwedge, normalized by the average value for each step. The average FOM values ranged from 0.2 (step 0) to 0.011(step 4). Imaging data from the 5 cm 50/50 phantom.

11

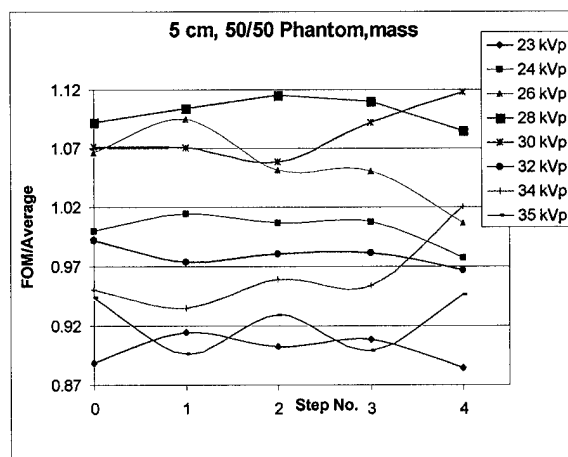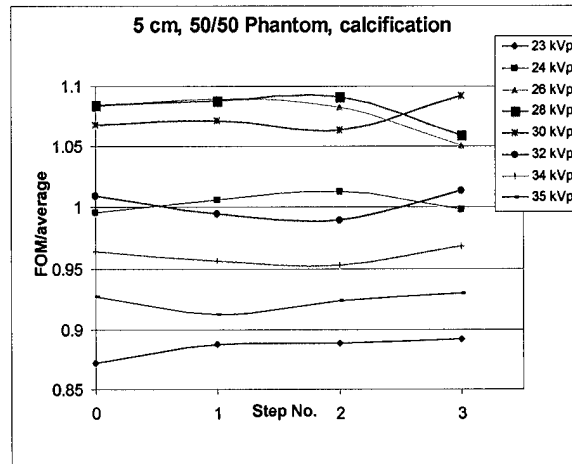**5 cm, 50/50 Phantom, calcification**

Figure 13: FOM values for the four steps
of the calcification stepwedge,
normalized by the average value for each
step. The average FOM values ranged
from 1.4 (step 0) to 0.64 (step 3). Data
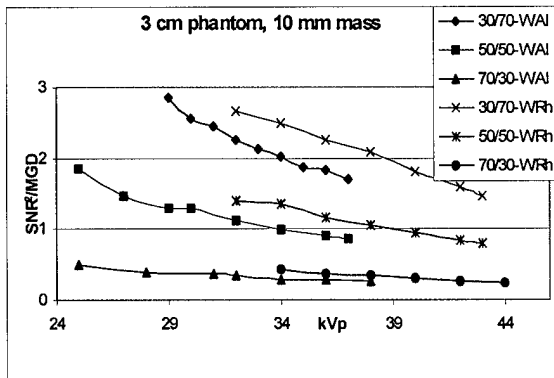are imaging the 5 cm 50/50 phantom.

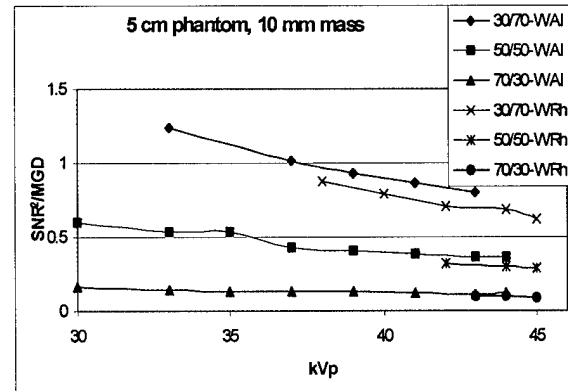Figure 14: FOM vs kVp for 3 cm thick
phantoms of three compositions.

Figure 15: FOM vs kVp for 5 cm thick
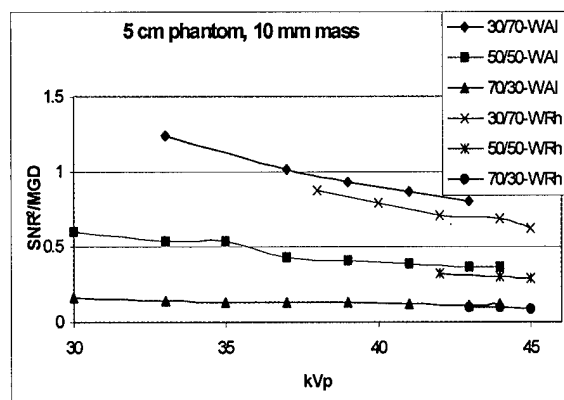phantoms of three compositions

Figure 16: FOM vs kVp for 7 cm thick
phantoms of three compositions.

Task 4. Optimize mAs, kVp, and Filter Selection Based on the Results of the Pre-exposures.

Optimization is based on maximization of the figure of merit: $FOM=(SNR^2/MGD)$. We have used the added information provided by the spatially varying signal levels in the pre-exposure ROIs to calculate a more refined estimate of the MGD than is possible using simply compressed thickness. To do this, the mean pixel value in each ROI is used to determine the relative transmission through the breast at that location. In regions of uniform thickness (all regions whose entrance surface is in direct contact with the compression paddle), variations in x-ray transmission are due to variations in breast composition. The region of the breast above each ROI is assumed to consist of two skin and subcutaneous layers with a uniform mixture of adipose and fibro-glandular tissue in between. The x-ray transmission through each region determines an adipose/fibroglandular composition ratio. Thus, for a given kVp, filter, and mAs, the MGD for the region of the breast above each ROI can be calculated separately, and the result summed to obtain an average MGD.

Preliminary Results: Task 4:

Software has been developed for analysis of digitally acquired mammograms. The primary two questions to be addressed by these analysis tools may be generalized as follows:

1) Which area of the digitally obtained mammogram contains the area of greatest radiographic attenuation (the ECROI)?
2) What portion of the pixel variance in the ECROI is a result of differential breast attenuation (signal) as opposed to random fluctuations (noise)?

With respect to question 1), the immediate objectives of these programs are:

1) Evaluate the correlation between the number of regions of interest (ROIs) sampled and the correct identification of the ROI containing the area of greatest radiographic attenuation (the ECROI)
2) Evaluate the correlation between ROI size and correct identification of the ECROI

13

3) Examine the effect of pixel binning on correct identification of the ECROI

Figure 17 below shows an example of a digitally obtained mammogram in which a 6 x 8 grid of ROIs has been established. The figure shows the mammogram, labeled with numbers whose locations correspond to the centers of the ROIs.
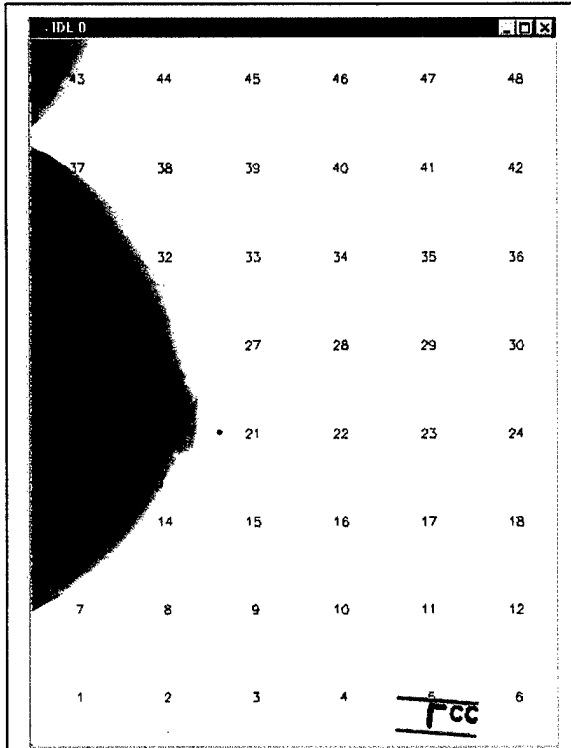
Figure 17: A digitally acquired mammogram, annotated with the locations of a 6 x 8 square grid of ROIs. The numerals are located at the centers of the square ROIs. The ROI positions are held fixed, while their side lengths are varied between minimum values of approximately 1.7% of the short dimension of the image, to their maximum value, equal to the center-to-center ROI spacing.
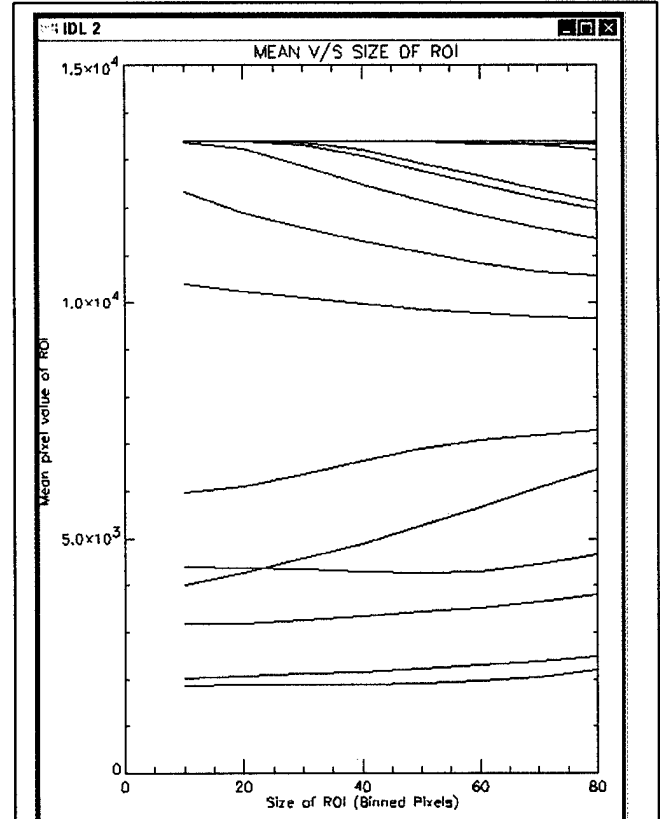
Figure 18: Average pixel value in the 48 ROIs of Figure 1, plotted as a function of ROI side length, in units of binned pixels. For the example shown, the ECROI (that with the lowest average pixel value) is the same for all ROI sizes tested. Its center is at the position labeled '19' in Figure 17. ROIs whose average pixel value is always large and constant (top of the graph) are located outside the region of the breast.

Figure 18 is a plot of the mean values of each ROI, plotted as a function of ROI size. The ROI with the lowest value is the ECROI. For the example shown, the ECROI is ROI #19. The contour plot of the pixel values, shown below in Figure 19, verifies that this is in fact the most highly attenuating portion of the breast.
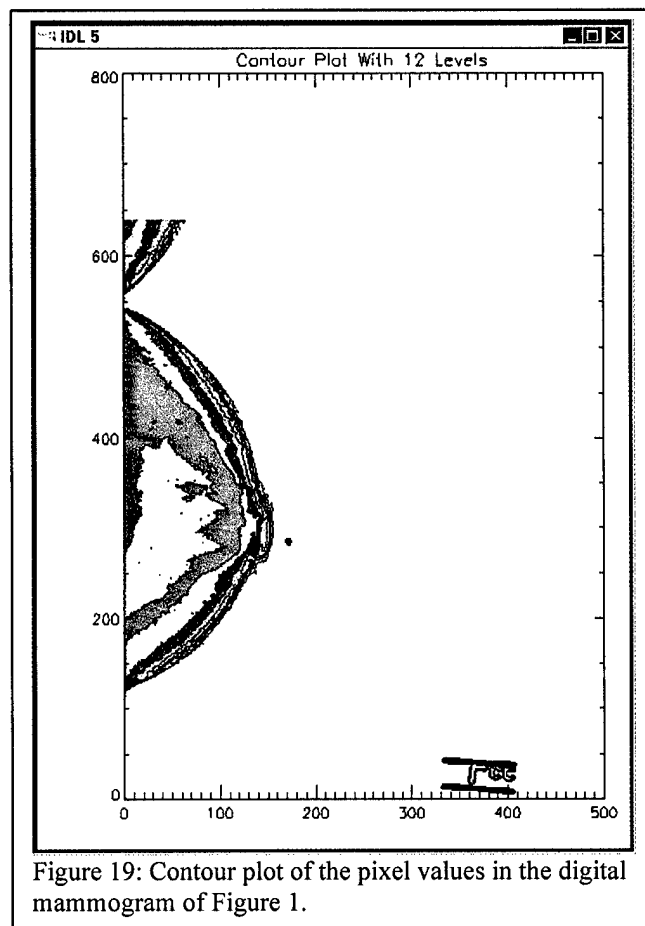
Figure 19: Contour plot of the pixel values in the digital mammogram of Figure 1.

Ongoing work

We are now in the process of running our analysis tools using digital mammograms obtained from breasts with a variety of compositions and sizes. We will evaluate the effect of radiographic heterogeneity on the selection of the ECROI, as well as possible spurious results from microcalcification clusters or cysts.

We are also developing analysis programs for determination of the pixel variance due to differential breast attenuation, and are characterizing intrinsic detector noise.

Using the data obtained from our experiments to date, we have implemented an automatic exposure control device onto the digital mammography system that will be refined during the remaining 6 months of support from this grant. Table 1 illustrates the technique factors and dose generated by the AEC of a conventional screen-film unit compared with those generated by the AEC implemented on our digital mammography system for patients undergoing both studies. Similar or reduced mean glandular doses were produced by the AEC implemented on the digital system, with one exception.

TABLE 1. Screen-Film versus Digital Exposure Factors and Dose for 16 Patients Undergoing Both Examinations

	SFM	ROOM	kVp	mAs	CM	MGD	total MGD	FILM SIZE	BR DENSITY	DIGITAL	kVp	mAs	CM	MGD	total MGD
1	LCC		26	316	4.7	574				LCC	26	218.4	7	366	
	RCC	seimens	26	179	4.1	391				RCC	26	160.1	6	303	
	LMLO		26	434	5.7	676				LMLO	26	156.4	6	303	
	RMLO	4174	26	298	4.5	538	2179	10X12	HD=3	RMLO	26	170.5	6	341	1313
2	LCC		27	177	4.8	386				LCC	27	70.2	5	155	
	RCC	MIV	25	191	4.5	290				RCC	25	70.2	5	155	
	LMLO		29	197	5.9	438				LMLO	29	141.3	6	265	
	RMLO	RM 3	30	170	5.7	407	1521	10X12	HD=3	RMLO	30	129.8	5	266	841
3	LCC		28	160	4.8	398				LCC	28	146	5	285	
	RCC	MIV	27	172	5	386				RCC	27	138.4	5	285	
	LMLO		30	133	5.9	317				LMLO	30	213.3	5	449	
	RMLO	RM 3	29	175	5.5	395	1496	8X10	HD=3	RMLO	29	179.7	5	367	1386
4	LCC		28	161	4.1	559				LCC	28	216.3	5	449	
	RCC	seimens	27	116	3.9	365				RCC	27	172.6	5	367	
	LMLO		27	46.9	2.5	191				LMLO	27	190	5	312	
	RMLO	4176	31	123	5.3	432	1547	10X12	XD=4	RMLO	31	127.4	5	303	1431
5	LCC		26	261	3.9	680				LCC	26	144.4	5	298	
	RCC	seimens	26	142	2.9	458				RCC	26	117	5	255	
	LMLO		26	243	3.1	785				LMLO	26	129.6	4	307	
	RMLO	4176	26	283	3.5	732	2655	8X10	XD=4	RMLO	26	114.2	4	307	1167
7	LCC		26	52.8	4.2	131				LCC	26	86.6	5	184	
	RCC	seimens	28	49.7	3.5	131				RCC	28	86.5	5	184	
	LMLO		28	48.6	3.7	131				LMLO	28	75	4	196	
	RMLO	4176	28	37.5	3.4	131	524	8X10	HD=3	RMLO	28	85.2	5	184	748
8	LCC		25	160	4.2	282				LCC	25	96.2	5	195	
	RCC	MIV	25	168	4.5	232				RCC	25	131.2	4	330	
	LMLO		25	208	4.5	290				LMLO	25	121.7	4	282	
	RMLO	RM 3	25	198	4.8	290	1094	8X10	HD=3	RMLO	25	114.3	4	282	1089

#	Device	View	31	48.9	3.6Rh	317	Total	Film	Proc	View	31	100.9	4	255	Total
9	M IV	LCC	31	48.9	3.6Rh	317				LCC	31	100.9	4	255	
		RCC	25	177	3.8	317				RCC	25	81	3	256	
	RM 3	LMLO	25	159	3.9	282		8X10	HD=3	LMLO	25	66	3	224	
		RMLO	25	176	4	317	916			RMLO	25	70.7	3	224	959
10	M IV	LCC	27	149	5.6	305				LCC	27	205.6	6	332	
		RCC	28	150	7.1	353				RCC	28	140.9	9	193	
	RM 3	LMLO	28	192	7.3	442		10X12	HD=3	LMLO	28	374.1	8	524	
		RMLO	28	155	7.2	353	1453			RMLO	28	447.4	9	634	1683
11	seimens	LCC	27	112	1.4	207				LCC	27	100.3	4	245	
		RCC	27	113	1.7	208				RCC	27	79.8	4	196	
	4176	LMLO	27	158	2	311		10X12	HD=3	LMLO	27	94.2	4	221	
		RMLO	27	173	2.2	312	1038			RMLO	27	93.4	4	221	883
12	M IV	LCC	25	188	4	317				LCC	25	65.1	3	215	
		RCC	29	62.4	3.3Rh	202				RCC	29	56.7	3	185	
	RM 3	LMLO	25	215	4	388		8X10	HD=3	LMLO	25	59.3	3	185	
		RMLO	25	198	3.8	352	1259			RMLO	25	59.4	3	185	770
13	M IV	LCC	25	119	4.5	174				LCC	25	157.1	4	312	
		RCC	25	133	4	247				RCC	25	129.6	4	234	
	RM 3	LMLO	25	78.4	3.9	141		8X10	HD=3	LMLO	25	90.7	3	221	
		RMLO	25	82.4	3.8	141	703			RMLO	25	97.4	3	246	1013
14	seimens	LCC	27	141.9	3.8	472				LCC	26	306.5	4	585	
		RCC	28	98.7	4	337				RCC	26	338.7	4	624	
	4176	LMLO	27	137	3.8	472		8X10	XD=4	LMLO	26	199.5	3	492	
		RMLO	27	153	3.7	540	1821			RMLO	26	292.6	4	585	2286
15	seimens	LCC	28	114	4	419				LCC	26	196.8	5	323	
		RCC	28	165	5	466				RCC	26	215.8	6	302	
	4174	LMLO	28	342	6.2	849		10X12	HD=3	LMLO	26	293.6	6	411	
		RMLO	28	254	5.8	649	2383			RMLO	26	329.2	6	439	1475
16	M IV	LCC	25	150	4.4	282				LCC	27	119	4	282	
		RCC	25	208	5	290				RCC	27	178	5	351	
	RM 3	LMLO	25	152	4.7	232		8X10	HD=3	LMLO	27	87	4	212	
		RMLO	25	196	5	290	1094			RMLO	27	98	4	235	1080

Reportable Outcomes:

Abstracts & Presentations:

The 1999 Radiological Society of North America, Chicago, IL, November 27- December 3, 1999: "Development of a quality control system for full-field digital mammography".
MJ Yaffe, MB Williams, LT Niklason, GE Mawdsley, AD Maidment, Radiology 209(P) (1999) 160.

The 5th International Workshop on Digital Mammography, Toronto, CA, June 11-14, 2000: "Beam Optimization for Digital Mammography". MB Williams, M More, V Venkatakrishnan, L Niklason, MJ Yaffe, G Mawdsley, A Bloomquist, A Maidment, D Chakraborty, C Kimme-Smith, LL Fajardo.

Publication:

Williams MB, Mangiafico PA, Simoni PU. Noise power spectra of images from digital mammography detectors. Med Phys 2000:6(7);1279-1293.

Conclusions:

The analysis of SNR and FOM as a function of kVp, shown in Figures 10 and 11, indicates that although the image SNR tends to decrease monotonically for all systems with increasing kVp, the accompanying MGD reduction results in fairly flat FOM curves. This is primarily due to tube loading, since it was not possible to obtain the same exit exposure at all kVps (that is, the tube output was insufficient to compensate for the lower transmission through the phantoms). Thus the falling SNR (and the falling MGD) with decreasing kVp are really consequences of falling exposure.

For a given phantom/technique combination, the SNR, and thus the *magnitude* of the FOM, increases with increasing step thickness for both types of stepwedge. However, the *shape* of the FOM vs. kVp curves for a given target/filter/phantom combination are essentially independent of step thickness, and are similar for mass and calcification equivalent signals. This is illustrated by the example shown in Figures 12 and 13. This implies that the result of the optimization is not sensitively dependent on signal amplitude.

Figures 14-16 illustrate a clear advantage to using rhodium filtration for thin breasts, but that for breasts 5 cm or thicker, aluminum filtration becomes increasingly advantageous. Similar statements can be made for the molybdenum target systems tested, where molybdenum filtration was superior for 3 cm phantoms of all compositions, but rhodium filtration produced better results for 5 and 7 cm thick phantoms of all compositions. These data suggest that the choice of external filtration is potentially more significant in determination of the overall FOM of a DM system than is choice of tube voltage.

Fahrig and Yaffe developed a model for optimizing spectral shape in digital mammography, and used it to calculate kVp values producing maximum SNR at a fixed dose for W and Mo spectra

18

[5]. They found that, for a fixed MGD of 0.6 mGy (60 mrads), the peak SNR occurred in the 24-31 kVp range (W spectrum) and 25-29 kVp range (Mo spectrum) for 4 – 8 cm breast thickness, and 50/50 breast composition. Their results were the same, whether the lesion type modeled was infiltrating ductal carcinoma or microcalcification.

Jennings et al. used a computational approach to identify maximum FOM values (FOM = SNR^2/MGD) for a variety of target/filter combinations, and breast thicknesses [6]. They found that for a Mo/Mo beam used to image 3-6 cm, 50/50 breasts, the FOM peaks at 27-28 kVp, and changes slowly with changing kVp near the peak values. Very similar FOM vs. kVp curves were obtained for Mo/Mo, Mo/Rh, and W/Al spectra, applied to 6 cm thick, 50/50 composition breasts. The general trends in our data appear to be consistent with those of these previous studies.

Implementation of the first generation of automatic exposure control device on the digital mammography system results in images having satisfactory image quality, SNR and mean glandular dose. For 16 patients undergoing both conventional mammography and digital mammography, the implemented AEC for the digital system performed satisfactorily.

References

1. Rose A. Vision: Human and Electronic. Plenum Press, New York, N.Y., 1973.

2. Sobol WT and Wu, X. Parameterization of mammography normalized average glandular dose tables. Medical Physics 24(4), 547-555. 1997.

3. Stanton L., Villafana, T., Day, J., and Lightfoot, D. (1984). Dosage evaluation in mammography. Radiology 150, 577-584.

4. Boone, J. (1999). Glandular breast dose for monoenergetic and high-energy x-ray beams: Monte Carlo assessment. Radiology 213, 23-37.

5. Fahrig, R. and Yaffe, M. (1994). Optimization of spectral shape in digital mammography: Dependence on anode material, breast thickness, and lesion type. Med.Phys. 21, 1473-1481.

6. Jennings, R.L., Quinn, P.W., Gagne, R.M., and Fewell, T.R. (1993). Evaluation of x-ray sources for mammography. Proc SPIE 1896, 259-268.

Appendix
Publication Reprint

Noise Power Spectra of Images from CCD Based Digital Mammography Detectors

Mark B. Williams and Peter A. Mangiafico

University of Virginia, Department of Radiology, Charlottesville, VA 22908

ABSTRACT

Because image noise constitutes the fundamental limitation of perceptibility in a digital radiograph, noise characterization through estimation of the noise power spectrum (NPS) is a central component of the evaluation of digital x-ray systems. We begin with a brief review of the fundamentals of NPS theory and measurement, derive explicit expressions for calculation of the one- and two-dimensional (1-d and 2-d) NPS, and discuss some of the considerations and tradeoffs when these concepts are applied to digital systems. Measurements of the NPS of two detectors for digital mammography are presented to illustrate some of the implications of the choices available. One mammographic detector is part of an early commercial system, currently under initial clinical evaluation. The other detector is being developed under a collaborative effort between Brandeis University (Waltham, MA) and the University of Virginia (Charlottesville, VA). Two dimensional (2-d) noise power spectra obtained over a range of input fluences exhibit pronounced asymmetry between the orthogonal frequency dimensions. The 2-d spectra of both systems also demonstrate dominant periodic structures both on and off the primary frequency axes. Our measurements indicate that for these systems, 1-d spectra useful for the purpose of DQE calculation may be obtained from thin cuts through the central portion of the calculated 2-d NPS. On the other hand, low frequency spectral values do not converge to an asymptotic value with increasing slit length when 1-d spectra are generated using the scanned synthetic slit method.

I. INTRODUCTION

Because image contrast can be manipulated during the display of digitally acquired radiographic images, noise imposes the fundamental limitation to object perceptibility in a digital radiograph. Thus noise characterization plays an increasingly central role in the evaluation of system performance in medical imaging. Well-developed methods used for noise characterization in film-based systems are currently being reassessed and reformulated to accommodate both the different nature of the noise and to take advantage of the analytical tools available with digital processing. An indication of both the current interest level and lack of consensus regarding noise characterization is the recent establishment of an AAPM Task Group (#16) for Standards for Noise Power Spectrum Analysis.

The noise power spectrum (NPS) is a spectral decomposition of the variance. As such, the NPS of a digital radiographic image provides an estimate of the spatial frequency dependence of the pixel-to-pixel fluctuations present in the image. Such fluctuations are due to the shot (quantum) noise in the x-ray quanta incident on the detector, and any noise introduced by the series of conversions and transmissions of quanta in the cascaded stages between detector input and output. Examples of the latter are gain variances in the conversion of x-ray quanta to light quanta in a phosphor (or to electron-hole pairs in a solid state detector), statistical fluctuations in the transmission of optical quanta between a scintillator and a photodetector, and additive noise sources such as preamplifier noise. Because it gives information on the distribution in frequency space of the noise power, the NPS is a much more complete description of image noise than is quantification of integrated (total) noise via simple measurement of the rms pixel fluctuations. The total variance can be obtained by integrating the NPS over spatial frequency.

In this paper we discuss aspects of NPS estimation as applied to digital radiographic systems. We begin with a general review of pertinent definitions and relations, and discuss the most important considerations when applying spectral estimation techniques to digital radiographic systems. Mathematical derivations sufficient to provide the reader with tools for quantitative application of the concepts are given, with more detailed development available in the cited references. These techniques are then applied to the analysis of the noise properties of two developmental CCD-based detectors for full field digital mammography.

II. BACKGROUND

Linear systems analysis can be usefully applied to any radiographic system whose transfer characteristic between input and output is *linear* (or linearizable) and *stationary* (the transfer properties are independent of location at the input surface) [H.H. Barrett and W. Swindell, *Radiological Imaging: The theory of image formation, detection, and processing,*

New York, Academic Press, 1981., K. Rossmann, "The spatial frequency spectrum: A means for studying the quality of radiographic imaging systems", Radiology 90(1):1-13, 1968.]. In this formalism, signal and noise are typically decomposed into their Fourier components (although other bases can be used), and input and output relations are expressed in terms of the frequency space Fourier amplitudes. Digital radiographic systems such as the one considered here usually exhibit linear responses to the incident x-ray fluence over several orders of magnitude. The following analysis assumes that the detector is operated within its linear range. Because in a digital detector the analog (presampling) signal and noise propagated through the detector are sampled by the digital matrix at discrete points, the system response is not strictly shift invariant (unless shifts are by an integer number of pixels). The effects of digital sampling on the NPS are described below.

A random process such as the noise fluctuations in an image is considered (wide-sense) *statistically stationary*, if its autocorrelation function (see below) is independent of the particular data sample (e.g. the particular location in the image) used to obtain it. This is only strictly true in a radiographic image if a) noise samples are obtained from spatially uniform exposures, and b) the detector adds no spatially fixed correlated noise. Dobbins has shown that the presence of a deterministic signal in the image data used to estimate the NPS has no effect on the resultant spectral estimates [J.T. Dobbins, "Effects of undersampling on the proper interpretation of modulation transfer function, noise power spectra, and noise equivalent quanta of digital imaging systems", Med. Phys. 22(2), 171-181 (1995)]. One other important assumption concerning the noise is whether or not it is *ergodic*. The noise in an image is ergodic if expectation values (averages) obtained from data samples at various locations in the image are equivalent to ensemble averages obtained from repeated measurements under identical conditions at a single location. Ergodicity implies stationarity, but not necessarily vice versa. The assumption of ergodicity of the noise in uniform irradiation radiographic images is typically made, and permits averaging of spectra obtained from several areas of the image.

In a cascaded system such as a digital mammography detector, the output of one stage constitutes the input to the following stage. In a linear, shift invariant cascaded system, each of the independent stages are also linear and shift invariant. At the output of any given stage of a cascaded detector system, the minimum possible value of the NPS is that set by the (uncorrelated) Poisson variance of the output quanta, which is equal to the number of quanta. Building on the work of Rossmann [K. Rossmann, "Spatial fluctuations of x-ray quanta and the recording of radiographic motttle", Am. J. Roentgenol. 90, 863-869 (1963).] and Kemperman and Trabka [J.H.B. Kemperman and E.A. Trabka, "Exposure fluctuations in model photographic emulsions. II. Statistics due to intensifying screens", Photogr. Sci. Eng. 25, 108-111 (1981).], Rabbani et al. have developed expressions for the propagation of the NPS through cascaded linear systems [M. Rabbani, R. Shaw, and R. Van Metter, "Detective quantum efficiency of imaging systems with amplifying and scattering mechanisms", Opt. Soc. Am. A. 4(5), 895-901 (1987).]. Using moment generating functions, they show that noise generated during a stochastic amplification process in one stage (such as the conversion of a single absorbed x-ray photon to many visible photons) is effectively passed as signal to the subsequent stage. Furthermore, they show that in a stochastic scattering process, while correlated components of the NPS are reduced by the square of the modulation transfer function (MTF) associated with the blurring process, uncorrelated Poisson noise is transferred independently of the MTF. This *stochastic* type of blur has a different effect on the NPS than *deterministic* blur, in which both correlated and uncorrelated components of the NPS of the preceding stage are attenuated by the square of the blur MTF [I.A. Cunningham, M.S. Westmore, and A. Fenster, "Effect of finite detector element width on the spatial frequency dependent detective quantum efficiency", Proc SPIE 2432 143-151 (1995).]. Because the signal is also modulated by the blur MTF, deterministic blur does not degrade the signal to noise ratio. Visible photon scatter in a phosphor is an example of stochastic blur; the effect of the integrating aperture of the individual pixels in a digital system is an example of deterministic blur.

A. Direct and Indirect Methods of NPS Calculation

1. The NPS is defined as the Fourier transform of the autocorrelation function, defined in one dimension as [R.B. Blackman and J.W. Tukey, *The Measurement of Power Spectra*, (Dover Publications, Inc., New York, 1958), Chap. 1]:

$$C(x) = \lim_{X \to \infty} \int_{-X/2}^{X/2} I(x+\tau) I^*(\tau) \, d\tau \qquad (1)$$

where $I(x)$ is the value (pixel value for a digital image) of the one dimensional image at position x, and $I^*(x)$ is its complex conjugate. Since $I(x)$ is real, $I = I^*$. The Fourier transform of $C(x)$ is then:

$$S(u) = \int_{-\infty}^{\infty} C(x) e^{-2\pi i x u} \, dx$$

$$= \lim_{X \to \infty} \frac{1}{X} \int_{-X/2}^{X/2} I(\tau) \, e^{+2\pi i \tau u} \int_{-\infty}^{\infty} I(x+\tau) e^{-2\pi i x u} dx \left[e^{-2\pi i \tau u} \right] d\tau$$

$$= \lim_{X \to \infty} \frac{1}{X} I(u) \int_{-X/2}^{X/2} I(\tau) \, e^{+2\pi i \tau u} \, d\tau \qquad (2)$$

Inspection of equations (1) and (2) show that:

$$S(u) = FT\{C(x)\} = \lim_{X \to \infty} \frac{1}{X} |I(u)|^2 \qquad (3)$$

where $I(u) = FT\{I(x)\}$.

Thus the NPS may be calculated either from the Fourier transform of the autocorrelation function (the indirect method), or from the square of the modulus of the Fourier transform of the data itself (the direct method). Note that since the data $I(x)$ are real, that $I(-u)=I^*(u)$. That is, the NPS at a given negative frequency is equal in magnitude to the NPS at the corresponding positive frequency. Extending the expression of equation (3) to two dimensions:

$$S(u,v) = FT\{C(x,y)\} = \lim_{X,Y \to \infty} \frac{1}{XY} |I(u,v)|^2 \qquad (4)$$

With the advent of the Fast Fourier Transform (FFT) and fast computers, indirect calculation of the NPS via the autocorrelation function has largely been replaced by the direct method. This paper will discuss only the latter method.

B. One Dimensional NPS

The detective quantum efficiency (DQE) is perhaps the best single descriptor of radiographic detector performance. It quantifies how well the detector is able to transfer the signal to noise ratio (SNR) inherent in the x-ray fluence at its input to the resulting image. For most two dimensional digital imaging detectors, the DQE is a function of at least three independent variables: its two spatial coordinates, and the x-ray exposure. It is a function of a single spatial coordinate for the special case of detectors with an isoplanatic response. The DQE can be written [R. Shaw, "The equivalent quantum efficiency of the photographic process", J. Photogr. Sc. 11, 199-204 (1963), J.C. Dainty and R. Shaw, Image Science (Academic Press, New York, 1974) pg. 312.]:

$$DQE(u,v,\varphi) = \frac{(\varphi g)^2 \, C(u,v) MTF^2(u,v)}{S(u,v,\varphi) SNR_{in}^2} \qquad (5)$$

where φ represents the magnitude of the input x-ray fluence at the detector surface, g relates changes in the zero frequency output signal to that at the input (i.e. it is the system gain), C(u,v) is the Fourier decomposition of the input signal, MTF(u,v) is the detector modulation transfer function, and $S(u,v,\varphi)$ is the output noise power spectrum [J.M. Sandrik and R.F. Wagner, "Absolute measures of image quality in magnification radiography", Med. Phys. 9(4), 540-549 (1982).]. For a monochromatic input x-ray spectrum, or in the case of a photon counting x-ray detector, SNR_{in} is given by the magnitude of the input fluence, φ.

In part because illustration of DQE(u,v, φ) requires a 4-dimensional medium, DQEs of 2-d imaging systems are typically presented one spatial frequency coordinate at a time for clarity. By definition:

$$MTF(u,v)=|2dFT\{ psf(x,y)\} | \qquad (6)$$

where psf(x,y) is the spatial response of the detector to a point x-ray input, and 2dFT represents a two dimensional Fourier transform. The 1-d MTF is typically measured using a narrow slit or edge [I.A. Cunningham and B.K. Reid, "Signal and noise in modulation transfer function determinations using the slit, wire, and edge techniques", Med. Phys. 19(4), 1037-1044 (1992).], and is:

$$MTF(u) = FT\{lsf(x)\} = FT\{ \frac{d}{dx}[esf(x)] \} \qquad (7)$$

Since $lsf(x) = \int_{-\infty}^{\infty} psf(x,y)dy$, then

$$\int_{-\infty}^{\infty} \text{lsf}(x)\, e^{-2\pi i x u}\, dx = \left| \int_{-\infty}^{\infty} \{\text{psf}(x,y)\, dy\}\, e^{-2\pi i x u}\, dx \right| = \left| 2d\text{FT}\{\text{psf}(x,y)\} \right|_{v=0} = \text{MTF}(u,0) \qquad (8)$$

Equations (7) and (8) indicate that evaluation of FT{lsf(x)} yields MTF(u,0), and thus *the appropriate expression of the NPS for calculation of the single coordinate DQE is S(u,0)*. Similar arguments pertain to MTF(y) [B.H. Hasegawa, *The Physics of Medical X-Ray Imaging*, 2nd ed. (Medical Physics Publishing, Madison, WI, 1991)].

Up to now, most characterizations of S(u,0) (or S(0,v)) of either analog (film-based) or digital radiographic systems have been made using the synthesized slit method [W. Hillen, U. Schiebel, and T. Zaengel, "Imaging performance of a digital storage phosphor system", Med. Phys. 14(5), 744-751 (1987). H. Roehrig, L. Fajardo, and T. Yu, "Digital x-ray cameras for real time steroetactic breast needle biopsy", Proc. SPIE 1896, 213-224 (1993). A.D.A. Maidment and M.J. Yaffe, "Analysis of the spatial-frequency-dependent DQE of optically coupled digital mammography detectors", Med. Phys. 21(6), 721-729 (1994). W. Zhao, I. Blevis, S Germann, and J.A. Rowlands, "Digital radiography using active matrix readout of amorphous selenium: Construction and evaluation of a prototype real-time detector", Med. Phys. 24(12), 1834-1843 (1997).]. In the original development of the method in the analog context, the optical aperture of the microdensitometer used to measure the film optical density formed the slit. The methodology has since been applied to digital systems by forming an effective slit from rectangular groups of contiguous pixels. In either case, a long, narrow slit is scanned in steps in one direction over the image. At each step the average intensity in the slit (average transmitted light for a scanning microdensitometer, or average pixel value for a digital system), is recorded. In this way, a one dimensional data series is generated. The squared modulus of the Fourier transform of the series, after scaling, gives the measured 1-d NPS. In the limit of an infinitely long 1-d data series in the x-direction, the resulting NPS is [R.C. Jones, "New method of describing and measuring the granularity of photographic materials", J. Opt. Soc. Am. 45, 799 (1955). J.C. Dainty and R. Shaw, *Image Science* (Academic, London, 1974), pg. 279.]:

$$S_{ss}(u) = \int_{-\infty}^{\infty} S(u,v)\, |T(u,v)|^2\, dv \qquad (9)$$

where T(u,v) is the optical transfer function (OTF) of the slit, and where S$_{ss}$(u) is the 1-d NPS measured via the scanned slit method. If the slit is rectangular, with x-dimension w and y-dimension L, then its point spread function is:

$$h(x,y) = \left(\frac{1}{w}\text{rect}\frac{x}{w} \right)\left(\frac{1}{L}\text{rect}\frac{y}{L} \right) \qquad (10)$$

and therefore T(u,v) is:

$$T(u,v) = \text{FT}\{h(x,y)\} = \text{sinc}(wu)\, \text{sinc}(Lv) \qquad (11)$$

where the sinc function is defined as

$$\text{sinc}(x) = \frac{\sin \pi x}{\pi x} \qquad (12)$$

Equation (9) becomes:

$$S_{ss}(u) = \text{sinc}^2(wu) \int_{-\infty}^{\infty} S(u,v)\, \text{sinc}^2(Lv)\, dv \qquad (13)$$

If the slit width is chosen sufficiently narrow, then sinc (wu) ~ 1 within the range of u over which S$_{ss}$(u) is to be evaluated. In any case, correction of the measured NPS by this factor is straightforward. In a digital system, a synthesized slit of 1 x N$_L$ pixels constitutes sampling the presampling NPS (which already includes the smoothing effect of the nonzero pixel aperture), using a line of N$_L$ delta functions, at an interval in the scan direction equal to the pixel width, Δx. The N$_L$ sampled values are then averaged. Thus, sinc (wu) → sinc (0) = 1, and L = N$_L\Delta y$, where Δy is the pixel size perpendicular to the scan direction.

As L→∞, sinc^2(Lv) becomes sufficiently narrow that S(u,v) is approximately constant over the range of v (near v=0) in which sinc^2(Lv) is appreciably nonzero [J.C. Dainty and R. Shaw, *Image Science* (Academic, London, 1974), pg. 279], and

$$S_{ss}(u) = \int_{-\infty}^{\infty} S(u,v)\, \text{sinc}^2(Lv)\, dv \cong S(u,0) \int_{-\infty}^{\infty} \text{sinc}^2(Lv)\, dv = \frac{S(u,0)}{L} \qquad (14)$$

Thus the desired NPS is S(u,0) = LS$_{ss}$(u).

Substantial effort has been devoted to understanding the criteria for "sufficiently large L". Sandrick and Wagner studied the effect of varying slit length on the 1-d NPS of radiographic screen-film systems [J.M. Sandrick and R.F. Wagner, "Radiographic screen-film noise power spectrum: variation with microdensitometer slit length", Appl. Opt. 20(16), 2795-2798 (1981)]. The found that the magnitude of the low frequency NPS is underestimated if the slit length is insufficient, but that the low frequency components approach a limiting value as the slit length is increased. The slit length required for low frequency NPS values within 5% of the plateau value was dependent on the particular screen-film combination, but ranged between a value equal to the length of the scan and one nearly twice as long. Koedooder et al. developed an expression to numerically approximate the integral in equation (13) [K. Koedooder, J. Strackee, and H.W. Venema, "A new method for microdensitometer slit length correction of radiographic noise power spectra", Med. Phys. 13(4), 469-473 (1986)]. The technique is applicable only to systems with rotational symmetry.

An alternate to the scanned slit approach is to extract a slice along one of the primary spatial frequency axes from the 2-d NPS. However, because these slices contain noise power from the orthogonal dimension near and at zero frequency, low frequency trending effects in the data can dominate their magnitude unless these trends are first removed. For this reason, the limited number of studies employing this approach have used "thick" slices made by extracting NPS data near to, but not directly on, the primary axes [J.T. Dobbins III, D.L. Ergun, L. Rutz, D.A. Hinshaw, H. Blume, and D.C. Clark, "DQE(f) of four generations of computed radiography acquisition devices", Med. Phys. 22(10), 1581-1593 (1995), R.J. Jennings, H. Jafroude, R.M. Gagne, T.R. Fewell, P.W. Quinn, D.E. Steller Artz, J.J. Vucich, M.T. Freedman, and S.K. Mun, "Storage-phosphor-based digital mammography using a low-dose x-ray system optimized for screen-film mammography", SPIE 2708, 220-232 (1996).]. As will be demonstrated below, in some digital detectors this approach can overlook structures that occur only at zero frequency in the orthogonal dimension.

C. Digital Noise Power Spectrum

In the above expressions, the 1-d and 2-d NPS are written as functions of a continuous variable, I, that describes the point-to-point fluctuations in the image, In a digital system, this continuous function of the spatial coordinates is sampled at regular intervals, Δx. Thus I is evaluated at a set of discrete locations, $x=n\Delta x$, $n=0,1,2,...N$, where $X=N\Delta x$. Correspondingly, functions of the spatial frequency variable u are now discrete; $u=k\Delta u$, $k=0,1,2,...K$, where $K\Delta u$ is the maximum spatial frequency sampled. This maximum measurable frequency, the Nyquist frequency, is $u_N \equiv K\Delta u = 1/(2\Delta x)$. To calculate the digital NPS, the above continuous expressions must be rewritten in terms of discrete variables. With the preceding definitions, equation (3) can be written:

$$S(k\Delta u) = \lim_{N\Delta x \to \infty} \frac{1}{N\Delta x} \left| \Delta x \sum_{n=0}^{N-1} I(n\Delta x) e^{-2\pi i (k\Delta u)(n\Delta x)} \right|^2$$

$$= \lim_{N\Delta x \to \infty} \frac{\Delta x}{N} \left| \sum_{n=0}^{N-1} I(n\Delta x) e^{-2\pi i (k\Delta u)(n\Delta x)} \right|^2 \qquad (15)$$

where N is the number of samples in the interval X. Similarly, equation (4) for the 2-d NPS becomes:

$$S(k\Delta u, l\Delta v) = \lim_{\substack{N\Delta x \to \infty \\ M\Delta y \to \infty}} \frac{\Delta x}{N} \frac{\Delta y}{M} \left| \sum_{n=0}^{N-1} \sum_{m=0}^{M-1} I(n\Delta x, m\Delta y) e^{-2\pi i [(k\Delta u)(n\Delta x)+(l\Delta v)(m\Delta y)]} \right|^2 \qquad (16)$$

The experimentally determined estimate of the digital NPS differs from the underlying analog spectrum in the following ways:

a) the noise has been convoluted with the rect (boxcar) function given by the pixel aperture (deterministic blurring)
b) the noise data has been sampled at discrete intervals given by the pixel center-to-center spacing (equivalent to multiplication by a comb function)
c) the record (image data) used to compute the estimate has been truncated from its original infinite length to a length given in each dimension by the number of points times the sampling interval (equivalent to multiplication by a 2-d boxcar function of dimensions $N\Delta x \times M\Delta y$)

The result of a) is the multiplication of the analog NPS with the absolute square of the 2-d sinc function that is the Fourier transform of the pixel aperture function. The result is often referred to as the *presampling* NPS:

$$S_{pre}(u,v) = S(u,v) \left| ab \, \text{sinc}(au) \, \text{sinc}(bv) \right| \qquad (17)$$

where S(u,v) is the analog NPS, and a and b are the pixel aperture dimensions.

The result of b) is that the presampling NPS is convoluted with the transform of the sampling comb function:

$$S_d(u,v) = S_{pre}(u,v) \otimes \otimes III(u,v; \frac{1}{\Delta x}\frac{1}{\Delta y})$$ (18)

where Δx and Δy are the sampling intervals in the x and y dimensions, and $\otimes \otimes$ denotes two dimensional convolution. Note that this comb function consists of an infinite array of delta functions separated in each dimension in frequency space by two times the respective Nyquist frequencies; $u_N = \frac{1}{2}\Delta x$, $v_N = \frac{1}{2}\Delta y$. $S_{dig}(u,v)$ is therefore an infinite 2-d array of replications of $S_{pre}(u,v)$, with the origin of each S_{pre} separated by $2u_N$ in the u direction and $2v_N$ in the v direction. This replication means that noise beyond the Nyquist frequency overlaps noise below the Nyquist frequency of adjacent replications. This overlap, or *aliasing*, becomes increasingly severe as the sampling interval is increased, that is as S_{pre} is increasingly undersampled. Because the phases of the Fourier components of the image noise are random, the presampling NPS cannot be directly measured using fine sampling techniques such as those commonly employed to measure the presampling MTF [H. Fujita, D. Tsai, T. Itoh, K. Doi, J. Morishita, K. Ueda, and A. Ohtsuka, "A simple method for determining the modulation transfer function in digital radiography", IEEE Trans. Med. Imag. 11(1), 34-39 (1992)].

Using digitized screen-film images, Giger et al. have studied the effects on the digital NPS of the sizes of the integrating pixel aperture and the sampling interval [M.L. Giger, K. Doi, and C.E. Metz, "Investigation of basic imaging properties in digital radiography", Med. Phys. 11(6), 797-805, 1984.]. Their results show that aliasing of high frequency noise (due, for example, to the high frequency components of x-ray quantum noise) above the Nyquist frequency can form a significant component of the measured digital NPS. Large integrating aperture size (i.e. larger than the sampling interval) tends to reduce the effect of this aliasing by smoothing the high frequency x-ray quantum noise, at the expense of spatial resolution. Aperture sizes less than the sampling distance increase the overall noise level, and particularly so at high frequencies. Dobbins has recently discussed the impact of undersampling on the interpretation of the MTF of digital systems [J.T. Dobbins, "Effects of undersampling on the proper interpretation of modulation transfer function, noise power spectra, and noise equivalent quanta of digital imaging systems", Med. Phys. 22(2), 171-181 (1995)].

The result of c) is that the NPS is also convoluted with the square of the transform of the data window, w(x,y):

$$S_{d,w}(u,v) = S_d(u,v) \otimes \otimes |W(u,v)|^2$$ (19)

where $S_w(u,v)$ is the measured NPS, and the frequency window, $W(u,v)$ is the Fourier transform of the data window, w(x,y) [N.C. Geckinli and C. Yavuz, *Discrete Fourier Transformation and Its Application to Power Spectra*, (Elsevier, Amsterdam 1983) pg. 99].

If the data series is simply truncated after N x M points, corresponding to multiplication of the infinite data sequence by a unity height box of dimensions $N\Delta x \times M\Delta y$, then the NPS is convoluted with a frequency window with modulus:

$$|W(u,v)| = N\Delta x M\Delta y \frac{\sin(\pi N\Delta x u)\sin(\pi M\Delta y v)}{\pi^2 N\Delta x u M\Delta y v}$$ (20)

A variety of data windows have been studied in many signal processing contexts, with the optimum choice for a given situation depending on the characteristics of the particular spectrum being characterized. Selection of a data window is based on the shape and width of the resulting frequency window. In general, there is a compromise between the width of the central lobe and the magnitude and extent of any side lobes. A broad central lobe reduces spectral resolution, and significant side lobes produce *leakage*, wherein noise power from nearby frequencies are mixed in the convolution process. In the case of power spectra exhibiting strong periodic components, as is the case in many digital radiographic systems, minimization of side lobe magnitude is often necessary for distinguishing small amplitude features adjacent to large amplitude peaks [N.C. Geckinli and C. Yavuz, *Discrete Fourier Transformation and Its Application to Power Spectra*, (Elsevier Science Publishing Co. Inc., Amsterdam, 1983) Chap. 3., R.W. Ramirez, *The FFT: Fundamentals and Concepts*, (Tektronix, Inc., Englewood Cliffs, NJ, 1985) Chap. 7.].

D. Experimental Estimation of the Noise Power Spectrum

Because noise in a radiographic image arises from stochastic (random) processes, any realization (image) of the noise associated with those processes is merely a sample chosen from the ensemble of all possible samples. Thus there is an inherent statistical uncertainty in the representation of the underlying (true) population variance by that sample. In this regard, Fourier decomposition of image noise (such as is performed in determination of the NPS) is different from the decomposition of signal (such as is performed in determination of the modulation transfer function (MTF)), where amplitudes and phases are known and fixed. The variance in the spectral components of the measured NPS is independent of the number of data points (e.g. the number of pixels) in the sample used to calculate it, and for mean-zero,

normally distributed noise, results in a coefficient of variation (COV) of approximately unity for each spectral estimate, S(u,v). [R.F. Wagner and J.M. Sandrik, "An introduction to digital noise analysis", *from The Physics of Medical Imaging: Recording System Measurements and Techniques*, A. Haus, ed. (AIP, New York, 1979), Appendix A]. The variance (uncertainty) in the estimate can be reduced by sectioning the entire $N\Delta x \times M\Delta y$ noise record into a number of contiguous blocks, and averaging the spectra obtained from each (ensemble averaging). The COV of the final estimate decreases as the inverse square root of the number of determinations. However, the spectral *resolution* is inversely proportional to the number of data points used to generate each NPS. Thus for a fixed amount of data, there is a tradeoff between frequency resolution and variance in the final NPS estimate. For example, if N data points, spaced at an interval Δx, are used to calculate a 1-d NPS, then the spectral resolution and COV are respectively [R.F. Wagner and J.M. Sandrik, "An introduction to digital noise analysis", *from The Physics of Medical Imaging: Recording System Measurements and Techniques*, A. Haus, ed. (AIP, New York, 1979)]:

$$\Delta f = \frac{1}{N\Delta x} \quad ; \quad COV \cong 1.0 \qquad (21)$$

If these N points are divided into n successive sections, then the frequency resolution and COV become:

$$\Delta f = \frac{1}{\frac{N}{n}\Delta x} = \frac{n}{N\Delta x} \quad ; \quad COV \cong \frac{1.0}{\sqrt{n}} \qquad (22)$$

III. METHODS

A. Data Acquisition

Both mammographic systems utilize molybdenum target x-ray tubes, with molybdenum or rhodium filtration. Data were acquired using Mo/Mo spectra and a variety of kVp and mAs settings. A block of acrylic 3.8 cm thick and sufficiently large to cover the entire detector surface was used to create realistic spectral composition and scatter conditions. Detector entrance exposure was measured using an ion chamber placed behind the acrylic block, with corrections applied to account for slight differences between locations of the chamber and the detector entrance surface, relative to the focal spot. For each selected kVp and mAs, eight images were obtained. Results given here are for data taken from a selected CCD module (i.e. the data do not span module boundaries, nor are data from different modules of a given detector averaged). The data blocks were divided into the maximum number of contiguous sections consistent with the NPS estimation technique to be used (e.g. N x L pixel sections for a scan in the x-direction, or N x M pixels for a 2-d NPS calculation). Spectra calculated from each section, and for each of the eight images were then averaged. The final ensemble averaged NPS estimates were thus averages of ~ 300 – 1200 spectra, resulting in standard errors of ~3%- 6%.

B. Subtraction of Background Trends

Low frequency background trends, such as those from the x-ray source heel effect, are often present in the data. Although such trends may have significant Fourier components only at frequencies below the lowest measurable frequency in the power spectrum ($1/N\Delta x$), leakage into low frequency spectral components can artificially inflate the low frequency NPS. For this reason, noise power spectra are frequently obtained by first subtracting one uniform exposure image from another made with the same exposure, and dividing the NPS resulting from the subtracted image by two. The factor of two accounts for the fact that the variance in the subtracted image gets approximately equal contributions from the uncorrelated noise in the two original images. Alternately, a difference image may be obtained by subtracting a highly averaged uniform exposure image from a single image. The random noise in the highly averaged image is negligible if a sufficient number of images are used to obtain it.

The image subtraction technique has the drawback, however, of also removing any uncorrected fixed pattern noise occurring at higher frequencies. Thus, this method may not be optimum for measuring the NPS of images that have already been uniformity corrected (flat fielded), because noise removed in the subtraction process would nevertheless be present in clinical images. We have therefore chosen not to use image subtraction, but to remove low frequency background trends in other ways. Two methods have been evaluated: subtraction of a low pass filtered version of the image, and subtraction of a low order polynomial fit to the image. When using the first method, for simplicity a rectangular (boxcar) filter was used to filter the entire 2-d data set. Subtraction of the resulting filtered image from the original is equivalent to subtraction of a running local mean as has been employed for one-dimensional data by others [M.L. Giger, K. Doi, and C.E. Metz, "Investigation of basic imaging properties in digital radiography. 2. Noise Wiener spectrum", Med. Phys. 11(6), 797-805 (1984).]. Convolution in coordinate space with a rectangular filter is equivalent to multiplication in frequency space by a sinc function. The dimensions of the square filtration kernel were chosen sufficiently large that the first zero crossing of the resulting sinc function was at or below the minimum frequency sampled in the NPS. In the

26

second method of background trend subtraction, a 2-dimensional polynomial was first fit to each uniform exposure image, and subtracted. Both first and second degree polynomials were evaluated.

In order to compare the above two methods of background trend subtraction, a synthetic data set was created. The data consist of a DC (average) pixel value, a normally distributed random component, a periodic component (one in each dimension), a linear (ramp) component, and a 2nd order component. The digital value of pixel I(i,j) was computed as:

$$I(i,j) = d_1 \cdot [rand(i,j)] + d_2(i,j) \tag{23}$$

where the rand() operator generates one of a set of normally distributed random numbers with average zero and standard deviation one, d_1 is a scaling factor, and

$$d_2(i,j) = a_0 \sin(iu_p + \delta_u) + b_0 \sin(jv_p + \delta_v) + a_1 i + b_1 j + a_2 i^2 + b_2 j^2 + C_0 \tag{24}$$

where u_p and v_p are the spatial frequencies of the periodic components in the x- and y-directions, respectively, and δ_u and δ_v are phase factors. The constant C_0 sets the magnitude of the DC component, and the constants a_0, b_0, a_1, b_1, a_2, and b_2 set the magnitudes of the periodic, linear, and quadratic components in the x- and y-directions, respectively. Figure 1 is a grayscale plot of a portion of one of the synthetic data sets.

Figure 2 shows a semilog plot of four representative 1-d power spectra generated from synthetic data. The spectrum labeled with diamonds is that of a data set with no background trend ($a_1 = a_2 = b_1 = b_2 = 0$). The second spectrum, labeled with squares, is from the same data, but with linear and quadratic components added. The third and fourth spectra (triangles and crosses), are calculated following trend removal via subtraction of a least squares surface fit to a second order polynomial or by subtraction of a boxcar filtered version of the image, respectively. In this example, the boxcar filter was 64 x 64 pixels, the same size as the sections of data used to calculate the 2-d NPS. The spectrum obtained with no trend removal demonstrates substantial leakage of low frequency noise power into the frequency range of the periodic component. The figure shows that both trend removal techniques reduce the noise power sufficiently at low frequency to eliminate the effects of the leakage. The quadratic fit technique virtually restores the original NPS, a result not surprising given the quadratic nature of the trend.

Figure 3 also shows the effects of different trend removal techniques, this time using flat field image data obtained from one of the mammography detectors. The 2-d spectra were computed from the average of 648 128 x 128 pixel sections. Thin slices were extracted along the v-axis. Again, slices are shown from 2-d spectra following no trend removal, and following subtraction of either a fitted quadratic surface or a low-pass filtered data set. In addition, two different size convolution kernels for low pass filtering are compared. For a rectangular, n x m pixel convolution kernel of amplitude $(n\Delta x m \Delta y)^{-1}$, where Δx and Δy are the pixel size in the x- and y-dimensions, the trend-corrected NPS is given by:

$$S_{d,w,b} = S_{d,w}[1 - sinc(n\Delta x u) \, sinc(m\Delta y v)] \tag{25}$$

In order that only noise power close to DC is removed, one would like the term $sinc(n\Delta x u) sinc(m\Delta y v)$ to be appreciable only for very low frequency. Therefore, the quantities $n\Delta x$ and $m\Delta y$, corresponding to the reciprocal of the first zero crossings of the sinc functions in the two dimensions, must be sufficiently large compared to the lowest frequency of interest in the NPS. In Figure 3, $S_{d,w,b}$ is shown for n=m=100, and for n=m=200. Note that for m=100, the first zero crossing of $sinc(m\Delta y v)$ is at a slightly *higher* frequency than the lowest frequency ($v=1/(128\Delta y)$) in the spectrum. The effect is a slight reduction in the noise power at the lowest frequency, relative to that shown for m=200. Because of this, in general we have found the best results by making the size of the smoothing kernel somewhat larger than the size of the blocks used to calculate the individual 2-d spectra.

It should be noted that 2-d quadratic fitting carries a significantly higher cost in processing time than does 2-d smoothing. This is true even if the fits are performed on the relatively smaller blocks individually, rather than on the full data set. For example, on a Sun Sparcstation 10 in our lab, trend removal using 2-d fits to 800 128 x 128 blocks takes approximately 4 hours of processing time, whereas the same amount of data can be smoothed in several minutes.

C. Units and Scaling

The noise power spectrum is more precisely termed the power spectral density, that is the noise power per unit frequency. [R.B. Blackman and J.W. Tukey, *The Measurement of Power Spectra*, (Dover Publications, Inc., New York, 1958), Chap. 1]. The quantity S(u,v) du dv is the contribution to the variance from noise components with spatial frequencies between u and u + du, and v and v + dv. The correct scaling of the NPS can be verified by observing that the volume (area) under the 2-d (1-d) NPS equals the total variance. Thus integration over frequency of spectra estimated using mean-zero sections from uniform illumination images should numerically equal the mean square deviations from their average of the pixel values in those sections.

Noise power spectra are sometimes presented normalized by the square of the large area (average) output signal [J.T. Dobbins III, D.L. Ergun, L. Rutz, D.A. Hinshaw, H. Blume, and D.C. Clark, "DQE(f) of four generations of computed radiography acquisition devices", Med. Phys. 22(10), 1581-1593 (1995), R.J. Jennings, H. Jafroude, R.M. Gagne, T.R. Fewell, P.W. Quinn, D.E. Steller Artz, J.J. Vucich, M.T. Freedman, and S.K. Mun, "Storage-phosphor-based digital mammography using a low-dose x-ray system optimized for screen-film mammography", SPIE 2708, 220-232 (1996).]. This normalization has the effect of compensating for differences in gain between two systems being compared, and of simplifying the expression for the DQE. With this normalization, equation (5) becomes:

$$DQE(u,v,\varphi) = \frac{C(u,v)MTF^2(u,v)}{\tilde{S}(u,v,\varphi)\,SNR_{in}^2} \tag{26}$$

where $\tilde{S}(u,v,\varphi) \equiv S(u,v,\varphi)/(\varphi g)^2$ is the normalized NPS.

IV. RESULTS

A. 2-dimensional NPS

The additive noise in the NPS obtained from a CCD-based digital mammography detector can be written as:

$$\sigma_a^2 = \sigma_t^2 + \sigma_r^2 + S_p(u,v) \tag{27}$$

where σ_t is the CCD thermal (Johnson) noise, σ_r is the read noise, and $S_p(u,v)$ is the variance due to frequency dependent periodic noise. Periodic noise can arise from capacitively coupled clock pulses, electromagnetic interference from power supplies, or 60 Hz pickup due to ground loops. Because the phase (in time) of such periodic interference is not fixed with respect to detector readout, its phase in the image is not fixed from frame to frame, and it is therefore not removed during the uniformity correction.

2-d spectra obtained from both developmental systems exhibit strong periodic structures over all exposure ranges tested. These structures take the form of sharp peaks in the spectra, and are due to periodic additive noise. Figure 4 shows grayscale plots of the 2-d spectra of one digital mammographic system at four exposure levels. Gridlines are spaced at one mm^{-1}. With increasing x-ray exposure, the periodic noise peaks are decreasingly apparent as the grayscale level is changed to accommodate the higher x-ray quantum noise contribution at low frequency.

B. Effect of Varying Slit Length on 1-d NPS

We have studied the effect of varying the length of the synthetic scanning slit used for the estimation of S(u,0) or S(0,v). Figure 5 shows 1-d spectra obtained from uniform illumination images using an exposure of 38 mR at the detector surface. Each of the spectra shown in the plot was generated by stepping a synthetic slit with x and y dimensions of 1 x L pixels, over the data in the x-direction in steps of one pixel. The longest slit length shown (L=512 pixels) corresponds to a slit approximately 20 mm long. At each step, the pixels in the slit were averaged. The resulting 128 element series was then Fourier transformed and scaled as follows to give the measured 1-d NPS. Combining equations (14) and (15) we have:

$$S(k\Delta u) = \lim_{\substack{N\Delta x \to \infty \\ N_L \Delta y \to \infty}} N_L \Delta y \frac{\Delta x}{N} \left| \sum_{n=0}^{N-1} I'(n\Delta x) e^{-2\pi i (k\Delta u)(n\Delta x)} \right|^2 \tag{28}$$

where $I'(n\Delta x) \equiv \frac{1}{N_L} \sum_{l=0}^{N_L-1} I(n\Delta x, l\Delta y)$ is the average of the pixel values in the synthetic slit. Note that from equation (16), a section of the digital 2-d NPS along the u-axis, calculated from a N x M section of the image, is:

$$S(k\Delta u,0) = \lim_{\substack{N\Delta x \to \infty \\ M\Delta y \to \infty}} \frac{\Delta x}{N} \frac{\Delta y}{M} \left| \sum_{n=0}^{N-1} e^{-2\pi i [(k\Delta u)(n\Delta x)]} \sum_{m=0}^{M-1} I(n\Delta x, m\Delta y) \right|^2 \tag{29}$$

For the special case when the slit length, $N_L\Delta y$, is equal to the scan length, $N\Delta x$, equations (28) and (29) reduce to the same expression:

$$S(k\Delta u,0) = \lim_{\substack{N\Delta x \to \infty \\ N_L \Delta y \to \infty}} \frac{\Delta x}{N} \frac{\Delta y}{N_L} \left| \sum_{n=0}^{N-1} e^{-2\pi i [(k\Delta u)(n\Delta x)]} N_L \, I'(n\Delta x) \right|^2 \tag{30}$$

Thus, for example, a cut along the u-axis from a 128 x 128 2-d NPS is identical to the 1-d NPS obtained by scanning a 1 x 128 pixel synthetic slit over 128 pixels in the x-direction. In all cases, we verified that the 1-d NPS obtained from the scanned slit method with the slit length equal to the size of the data block used to generate the 2-d NPS, was identically equal to the section from the 2-d spectrum along the u- or v-axis.

As shown in Figure 5, the very low frequency values of the 1-d NPS did not converge to a plateau value for slit lengths of up to 512 pixels, which is twice the scanned distance. This behavior is similar to that observed by Sandrik and Wagner for the Kodak Hi-Plus/XRP screen-film system. [J.M. Sandrik and R.F. Wagner, "Radiographic screen-film noise power spectrum: variation with microdensitometer slit length", Appl. Opt. 20(16), 2795-2798 (1981).]. In that study, measured NPS values at 0.39 cycles/mm continued to increase with increasing slit length up to L = 5.9 mm for scan a distance of 2.5 mm, while convergence to a plateau value was observed for other screen-film systems at similar frequencies.

C. Slices from the 2-d NPS

Notably in the context of the evaluation of storage phosphor systems, others have obtained 1-d spectral estimates by extracting thick cuts from the 2-d NPS. The cuts are made parallel to the primary axis of interest, but do not include the axis, so as to avoid low frequency trending effects. We have evaluated this approach for analysis of the spectra of the digital mammography systems. Figure 6 is a plot comparing a thin cut (a single frequency bin wide) along the primary (v) axis of the 2-d NPS with a thick cut generated by summing the two four-bin-wide sections immediately on either side of, and adjacent to, the v-axis. The thick slices adequately represent the on-axis slice except at low frequency, where the NPS decreases rapidly with increasing u. Of greater significance is the omission of the periodic noise structures near spatial frequencies of 3 and 6 cycles/mm. These represent noise power from fluctuations in the y-direction (left to right direction of the breast support) that are constant in the anterior-chest direction. Such noise may appear as horizontal stripes in the mammographic image.

As would be expected, thicker slices are poorer approximations to the on-axis cuts, as the falloff in the 2-d NPS in the dimension orthogonal to the slices causes the average spectral values to be reduced. This produces an effect similar to that resulting from utilization of a scanning slit of insufficient length.

D. NPS of the Developmental Mammographic Systems

The NPS of uniform illumination images from both digital mammographic systems was measured over a range of detector entrance surface exposures from 9 mR to 78 mR. For each exposure, 2-d noise power spectra estimates were made as described in Section III.A. Figure 7a) and 7b) are semilog plots of cuts along the u- and v-axes of both systems at four exposure levels. The spectra have been normalized by the respective large area output signal squared. Immediately apparent are the very different curvatures of the spectra obtained from the two systems, with the spectra of System 1 leveling off at high frequency, while those of System 2 continue decreasing out to the Nyquist frequency. At all exposures tested, the normalized noise power of System 2 is less than 10^{-6} at Nyquist. Also apparent from Figure 7 is the fact that the noise behavior of System 1 is different in the x- and y-dimensions, with the y-dimension exhibiting significantly greater noise at high frequency. In both systems, the y direction corresponds to the parallel transfer direction of the CCDs.

E. Comparison with Pixel Variance

Each of the 2-d spectra presented in this study was integrated over spatial frequency in order to compare the resulting value with the variance calculated from the pixel-to-pixel fluctuations. The integrals were calculated over the range from $-f_N$ to $+f_N$, where f_N is the Nyquist frequency. In all cases, differences between the integrals and the directly calculated total variance were less than 0.5%.

Figure 8 shows the total noise of the two digital mammography detectors over the range of exposures from 9 mR to 78 mR. The noise was determined from the square roots of the integrated volumes under the 2-d spectra whose axial slices are shown in Figure 7. The figure plots the log of the noise versus the log of the exposure. For both systems, straight lines have been fit to the experimentally determined data points, and the calculated slopes of the lines are shown in the figure. In a system for which x-ray quantum noise is the dominant noise source, the slope should be approximately 0.5.

V. DISCUSSION

Similarly to other types of radiographic systems, digital detectors for mammography can usefully be characterized through Fourier analysis of their noise characteristics. However, investigators preparing to estimate noise power spectra of such systems are confronted with a bewildering array of procedural considerations, ignorance of which can lead to misleading results. Because significant digital processing power is now available to the majority of medical physicists, limitations formerly imposed by the tradeoff between spectral resolution and uncertainty in the spectral estimates are much less

stringent than even a decade ago. Thus ensemble averaging over a large number of uniform exposure images is feasible, thereby permitting fairly subtle features of the NPS to be resolved. The necessary resolution is determined by the proximity in Fourier space of relevant features and should be determined on a system-by-system basis. For the digital systems characterized in this paper, 128 x 128 2-d spectra, yielding 64 frequency bins in the single-sided 1-d spectra, were sufficient to resolve the features of interest. Occasionally, we found it useful to recalculate particular spectra at higher resolutions. This may be useful, for example, for assurance that low frequency structures are in fact independent of background trend noise power residing in the lowest frequency bin (the range between zero and $1/N\Delta x$, where $N\Delta x$ is the length of the data series).

The noise power in images from both the digital mammographic systems has markedly non-isoplanatic properties, particularly at low exposure where frequency-dependent system noise is most predominant. Because the inherent nature of the CCD readout process defines orthogonal serial and parallel directions, image noise generated during the readout process is unlikely to fall along the $|u| = |v|$ lines of the 2-d NPS. Such noise can be due to digital clock pulses that are radiatively or capacitively coupled to the analog data signals. Furthermore, the majority of this noise power resides away from the principle spatial frequency axes, and thus does not appear on the 1-d NPS, whether it is obtained from an extracted slice of the 2-d NPS, or from a scanned slit. It is therefore important that the full 2-d NPS be estimated, even if 1-d spectra are subsequently used for SNR calculations.

The scanned slit method for obtaining 1-d spectra yielded results identical to those obtained from thin cuts through the 2-d spectra, except for the susceptibility of the former approach to slit-length-dependent variability in the low frequency components. The absence of convergence of the low frequency values of $S(u,0)$ reflects the peaked nature in the v-direction of the 2-d NPS, $S(u,v)$, near $v=0$. Since the value of $S_{ss}(u)$ obtained from scanning is scaled by L to get $S(u,0)$ (c.f. equation (14)), only for values of u where the addition to the integral of equation (13) is proportional to L will the result be insensitive to changes in L. Thus, approximating the function sinc^2 (Lv) as a triangle of base width 2/L and unity height centered at $v=0$, $S(u,0)$ obtained using a slit of length L_1 is approximately equal to that obtained with slit length L_2 only if $S(u,v)$ is approximately constant in the v-direction between $v=2/L_1$ and $v=2/L_2$. Note that, except for $u = 0$, where $S(0,v)$ is symmetric about the u-axis, this requirement must also be met between $v=-2/L_1$ and $v=-2/L_2$. Dainty and Shaw have recommended that the slit length be at least equal to the inverse of the frequency resolution (that is, at least equal to the scan distance). Our results indicate that for digital systems, a length significantly greater than the scan distance may be required for asymptotic convergence of the low frequency NPS estimates. In practice, the most direct method of determining sufficiently large L is probably inspection of cross-sectional cuts through the 2-d NPS, obtained at as high a frequency resolution as is practicable, bearing in mind the guidelines of the preceding sentences.

For the noise data studied here, subtraction of a duplicate data set that has been convoluted with a two-dimensional rect function kernel is an effective and efficient method for the removal of low frequency trending effects. The effectiveness of the technique is indicated by the similarity between thick slices extracted from the 2-d NPS near the central axes, and on-axis slices (c.f. Figure 6). Because the 2-d NPS can contain on-axis features not present in adjacent regions of frequency space, 1-d spectra obtained from thick slices parallel to the primary axis of interest may not be representative of the on-axis NPS. For this reason, thin on-axis cuts are recommended.

VI. CONCLUSIONS

Fourier analysis has been used to characterize the noise properties of two developmental detectors for digital mammography. The noise power spectra of images from the two systems exhibit several common features. They contain features that are strongly dimension-specific, and are often localized to relatively small portions of frequency space. They also contain predominant peaks indicative of periodic additive noise, both on and off the primary frequency axes. On the other hand, the noise properties of the two mammographic detectors differ significantly in some aspects. Over a range of input exposures, the spectra of System 1 are characterized by nearly constant noise power for frequencies greater than about 8 cycles/mm, while those of System 2 exhibit increasingly sharp fall off with increasing frequency. Cuts along the two primary axes of the 2-d NPS of System 1 exhibit very different shapes, while those of System 2 are nearly identical along the two axes. At all frequencies, the relative noise of System 2 decreases monotonically with increasing x-ray exposure, while that of System 1 reaches a minimum then begins to increase again. The overall noise of System one increases approximately as the square root of the number of incident x-ray quanta, while that of System 2 increases more slowly.

Because of the complex nature of the frequency distribution of the noise power in images from digital mammographic systems, analysis of the complete 2-d spectra, rather than only the 1-d spectra, is important. Straightforward removal of background trending artifacts is possible via a simple filtering process. Cuts obtained along the primary axes of the 2-d spectra can provide valid estimates of the 1-d NPS without the use of synthetic scanned slit techniques.
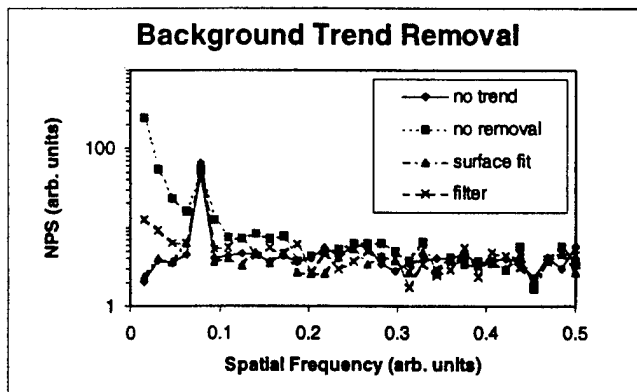
ACKNOWLEDGEMENTS
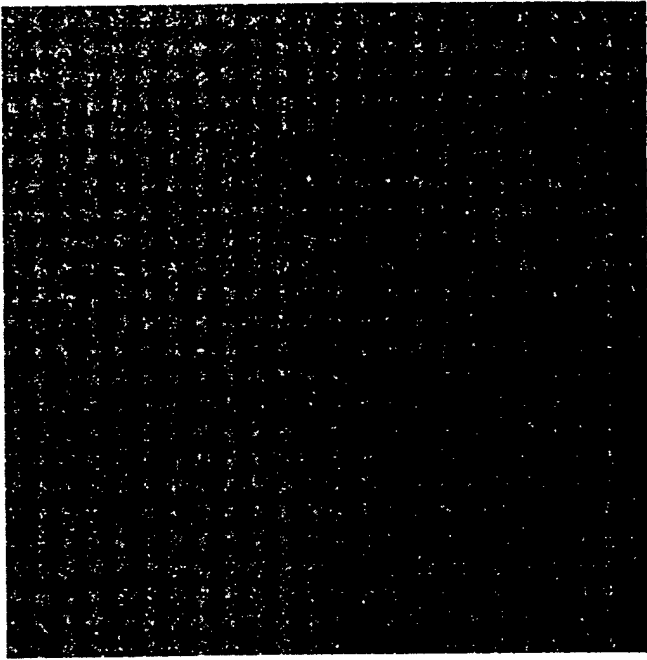
Figure 1
Grayscale image of a synthetic data set used to evaluate methods of background trend removal. For ease of visualization, the data set shown contains only sinusoidal, random, and DC components (no linear or quadratic component).

Background Trend Removal

Figure 2
Comparison of background trend removal techniques, using synthesized data set. The figure shows the NPS calculated from a) data with no background trend (diamonds), b) the same data as a), but with linear and quadratic trends added (squares), c) the same data as b), but after subtraction of a 2-dimensional second order polynomial fit to the data (triangles), and d) the same as b), but after subtraction of a low-pass filtered version of the data (crosses).

MEDICAL PHYSICS   Mark B. Williams, Ph.D.

Trend Subtraction
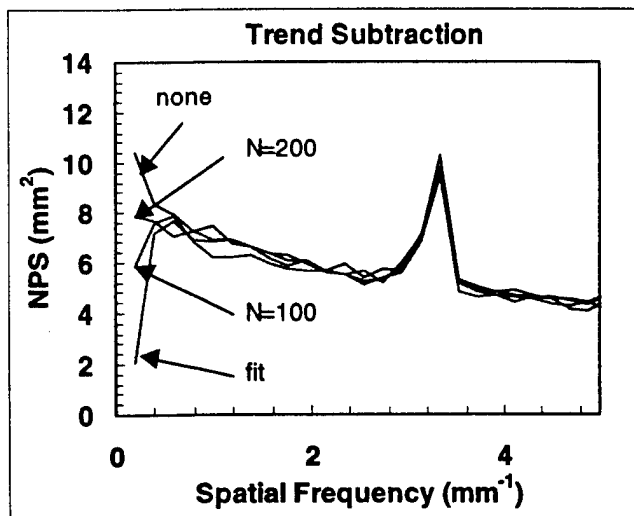
Figure 3
Comparison of background trend removal techniques, applied to images obtained with one of the digital mammography systems, obtained using nominally uniform illumination. The graph shows four 1-d power spectra, S(0,v), obtained from thin cuts from four different 2-d spectra. The 2-d spectra were calculated following a) no trend removal (none), b) subtraction of a fitted quadratic surface (fit), c) subtraction of a low pass filtered version of the data using a 100 x 100 pixel convolution filter, and d) same as c), but using a 200 x 200 pixel filter.

MEDICAL PHYSICS   Mark B. Williams, Ph.D.
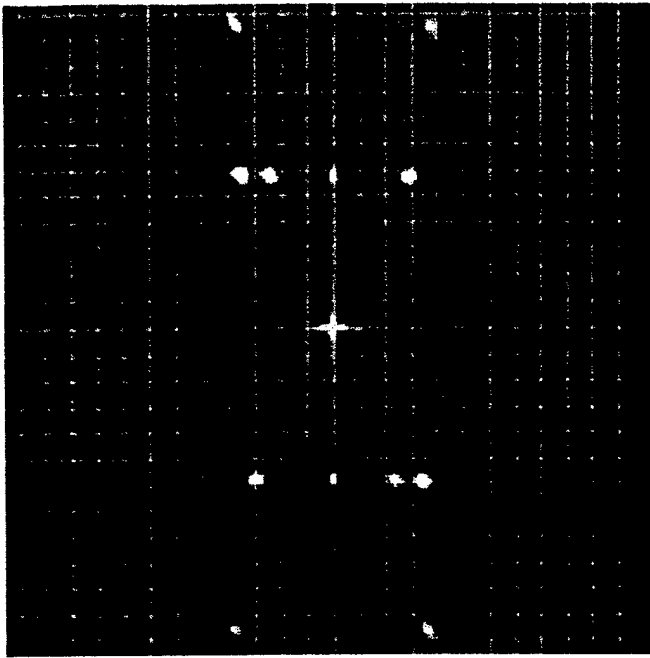
Figure 4a
2-d NPS at 9 mR exposure to the detector surface. Gridlines are spaced by 1 mm^{-1}.
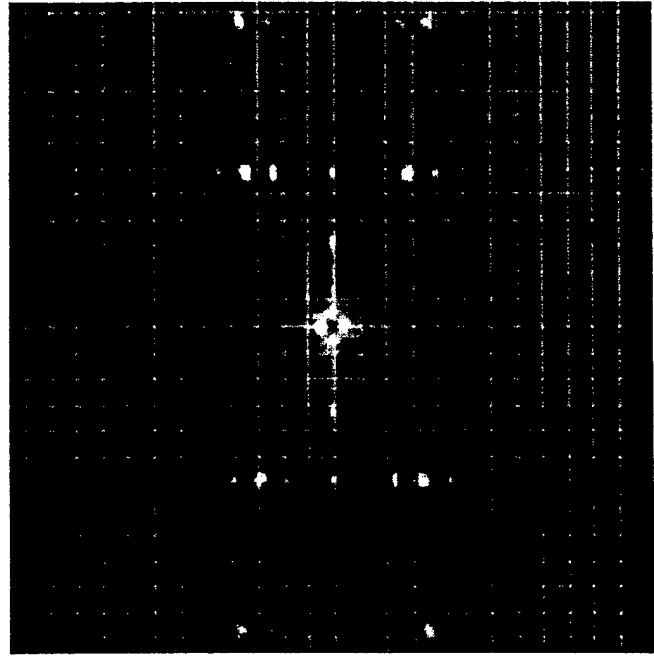
Figure 4b
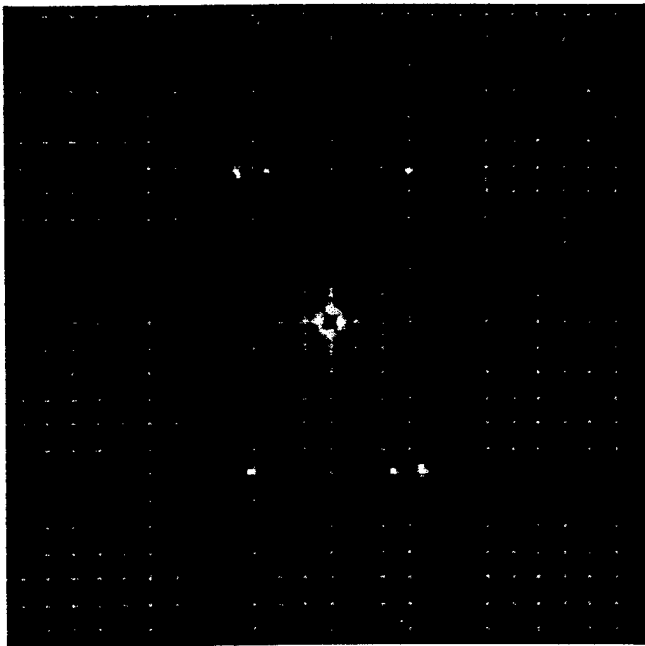2-d NPS at 18 mR exposure to the detector surface. Gridlines are spaced by 1 mm^{-1}.

Figure 4c
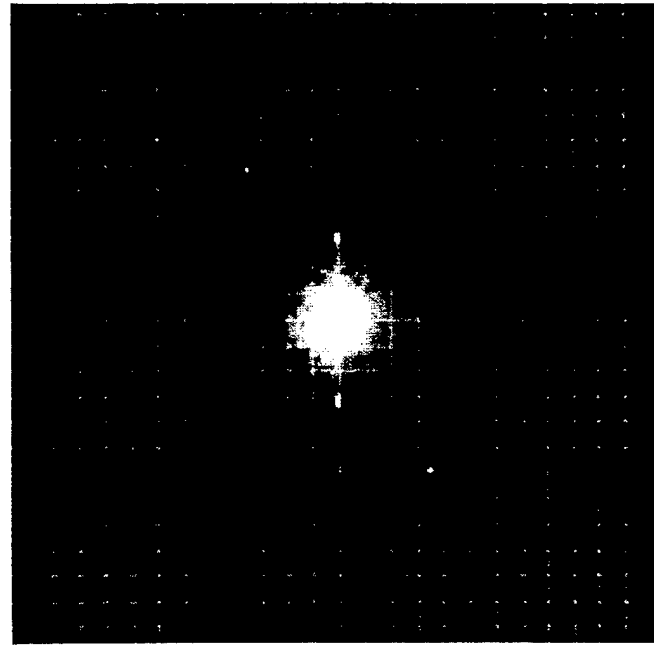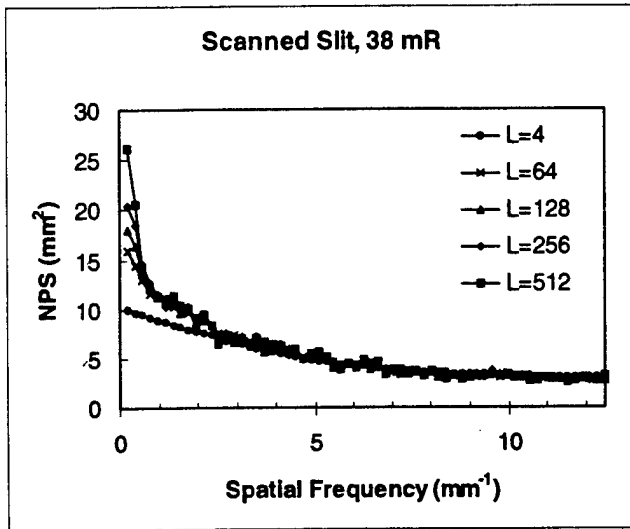2-d NPS at 38 mR exposure to the detector surface. Gridlines are spaced by 1 mm^{-1}.

Figure 4d
2-d NPS at 76 mR exposure to the detector surface. Gridlines are spaced by 1 mm^{-1}.

Scanned Slit, 38 mR

Figure 5
1-d noise power spectra obtained from the same data set, but with various scanning slit lengths. Spectral components above approximately 0.6 cycles per millimeter are insensitive to changes in slit length for slit lengths of 64 pixels or greater. However,
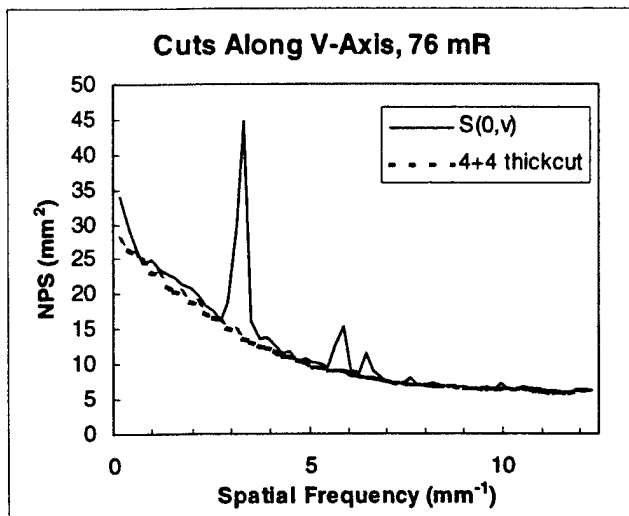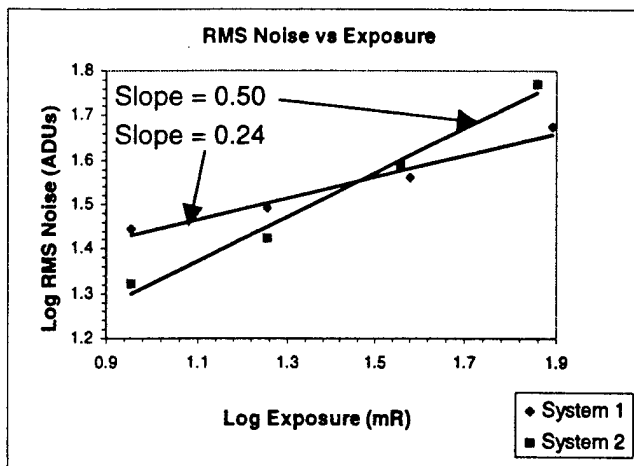
MEDICAL PHYSICS   Mark B. Williams, Ph.D.

Cuts Along V-Axis, 76 mR

NPS (mm²) vs Spatial Frequency (mm⁻¹)

Legend:
— S(0,v)
- - - - 4+4 thickcut

Figure 6

Slices from 2-d NPS of digital mammographic system. The solid line
is a slice one bin wide, along the v-axis. The dotted line is the sum
of two 4-bin sections taken from either side of the v-axis.
Differences between the two occur primarily at low frequency and
because of on-axis periodic noise components.
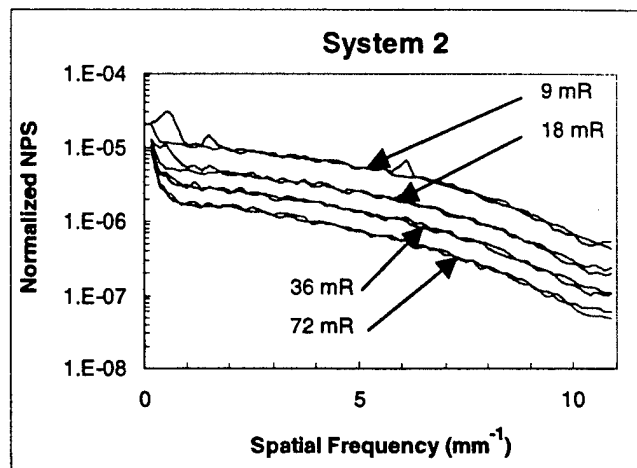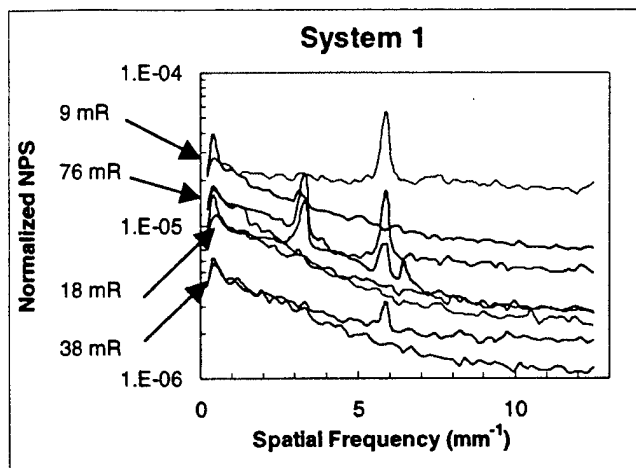
Figure 7
Noise power spectra of the two developmental digital mammography
systems studied. Spectra are shown at four exposures for each system.

RMS Noise vs Exposure

Slope = 0.50

Slope = 0.24

Log RMS Noise (ADUs)

Log Exposure (mR)

♦ System 1
■ System 2

Figure 8
Log noise vs log exposure for two digital mammographic detectors.
The noise was found from the square root of the integrated volume
under the 2-d NPS. The plot shows the slope of straight lines fit to the
measured data.

MEDICAL PHYSICS   Mark B. Williams, Ph.D.